A guide to wireless networking by light

Harald Haas [a,*], Cheng Chen [a], Dominic O'Brien [b]

[a] University of Edinburgh, King's Buildings, Edinburgh, EH9 3JL, UK
[b] University of Oxford, Parks Road, Oxford, OX1 3PJ, UK

ABSTRACT

The lack of wireless spectrum in the radio frequency bands has led to a rapid growth in research in wireless networking using light, known as LiFi (light fidelity). In this paper an overview of the subsystems, challenges and techniques required to achieve this is presented.

1. Introduction

Wireless data communication has become an essential utility in our private and business lives. There are more than 7 billion smartphones primarily used for personal communication. There is a sharp increase in the number of wearables such as smart watches, health trackers and digital glasses. The latter will drive new applications around virtual reality (VR), augmented reality (AR), high definition video streaming and Industry 4.0. In the future, there will also be 100 billion internet-of-things (IoT) devices that will underpin our smart homes and smart cities. Currently, all these digital wireless services use radio frequencies which are part of the wider electromagnetic spectrum. However, the lower frequency bands that are easy to use and have desirable propagation properties already have multiple uses. Consequently, there is very little spare resource to support the exponential growth in demand. The wireless community is working on multiple solutions to enhance wireless data transmission capabilities. For example, the new WiGig (wireless gigabit) systems, defined in IEEE 802.11ad and revised in 802.11ay, operate in the 60 GHz region and have access to around 14 GHz of bandwidth in the U.S.A. However, WiGig and other mmWave (millimeter-wave) radio frequency (RF) solutions (including the newest version of WiFi (wireless fidelity), 802.11ax) all exhibit similar challenges. For an RF link, the path loss is proportional to the square of the carrier frequency, and propagation becomes line-of-sight (LoS) or almost LoS. This means that moving wireless systems from the now 3 GHz region to the 60 GHz mmWave region will incur an additional path loss of 400, or 26 dB. Therefore, the high path loss along with the limited signal transmission power constraints require cells to be smaller, and beamsteering to direct energy from transmitter to receiver. In addition, the reliable coverage achieved with conventional cellular systems is much more difficult due to the LoS nature of the communications channel. There has been good technical progress to create the systems required to achieve this, with demonstrations at 30 GHz, and 60 GHz [1]. However, it is clear that these systems are complex. Furthermore, such high data capacity system does not easily provide the reliable, ubiquitous coverage that third generation (3G) and fourth generation (4G) cellular systems can deliver.

The optical spectrum offers a bandwidth which is many orders of magnitude greater than that the RF spectrum can offer. The visible and near infrared (IR) regions together are 2600 times larger than the 0–300 GHz RF spectrum. This spectrum is unlicensed and subject only to eye-safety regulations. Light emitting diode (LED) and laser sources are readily available across much of the spectrum, as are

---

* Corresponding author.
    E-mail address: h.haas@ed.ac.uk (H. Haas).

photodiodes to act as receiving elements. This makes optical wireless communication (OWC) systems, which includes the IR region, a potentially attractive medium for wireless communications [2].

Free-space point-to-point long distance optical wireless transmissions was the first OWC system to be considered, and this is known as free-space optical (FSO) communication [3]. A large body of work exists in this area, including commercial deployments, communications with mobile platforms [4], and increasingly communications in space [5]. Reference [6] provides a recent review of the field.

OWC technologies for short-range indoor applications were pioneered by the early work of Gfeller and Bapst, who demonstrated that a diffused IR radiation communication system could achieve data rates of around 100 kbps [7]. With the advancements of IR-based technology, the infrared data association (IrDA) formulated a set of protocols for wireless IR communications between electronic devices [8]. Such links were limited to several Mbps over ranges <1 m at wavelengths between 850 and 900 nm. More recently, work on very short distance IR links for cable replacement [9] has led to a 10 Gbit/s IR standard.

In addition to these cm-range links, a number of IR demonstration networks and systems concepts have been reported. Kahn and co-workers demonstrated a limited system operating at 50 Mbit/s [10], as well as introducing angle diversity concepts [11]. Imaging [10] and holographic [12] receiver designs have also been developed. Demonstration networks, operating at rates of up to Gbps have also been reported [13]. Reference [14] provides a recent review of the field. Eye safety regulations have led to a constraint on the amount of maximum emission power of the IR transmitter. Consequently, this has resulted in a limited link budget for IR networks. Therefore, it is not possible to cover typical indoor spaces with a single access point (AP) and achieve high data rates. Such rates, combined with good coverage requires multiple transmitters and receivers, which leads to complex systems that do not scale well as data rate increases. Using a limited number of narrow beam optical links within a room, and beamsteering to direct these to terminals allows data rates to scale. Furthermore, using light from optical-fibre systems combined with beamsteering has led to the highest rate indoor wireless links (RF or optical) demonstrated thus far. Recent demonstrations, operating at up to several hundred Gbit/s are reported in Refs. [15–17].

With the emergence of energy-efficient white-LEDs, solid state lighting (SSL) is gaining great popularity in the lighting industry [18]. It is expected that LED-based lighting infrastructures will replace all conventional lighting infrastructure in the coming decades. This trend provides a unique opportunity to create novel combined lighting and wireless communication networks. The use of LEDs for wireless data transmission is known as visible light communication (VLC) [19] which was first introduced by Nakagawa [20]. The wireless networking using VLC is referred to as LiFi, first introduced in 2011 [21]. During the last 10 years, there have been significant advancements in this field. The link data rates have increased three orders of magnitude from 10 Mbps in 2006 to 10 Gbps in 2016 [22,23], and in 2011, the Institute of Electrical and Electronics Engineers (IEEE) published the first standard for short-range VLC applications [24]. In the last 5 years, there has been a significant shift from point-to-point, static VLC systems to complete LiFi cellular systems. As a result, now there is a LiFi 'topic interest group' in IEEE 802.11, and this has now progressed to an IEEE 802.11 Study Group.

While IR networking requires dedicated infrastructure, VLC requires modification of an existing lighting system, thus offering potential cost-savings. Crucially, as detailed later in the paper, the level of illumination required for human users leads to a link margin many orders of magnitude superior to that in IR systems, enabling high data-rates with good coverage using simple components. These advantages, and others detailed elsewhere in the paper, have led to the rapid growth in this area.

This paper introduces the elements required and the challenges faced in creating LiFi networks. This paper does not attempt to provide a comprehensive overview of the field of VLC and LiFi (for these, the reader is referred to recent review papers [25–28] and references therein).

2. LiFi attocell networks

Fig. 1 illustrates the concept of a LiFi attocell (LAC) network. The room is lit by a number of light fixtures, which provide illumination and an optical AP to users within the illumination pattern of the light. The illumination can be modulated at high rates, not visible to the occupants of the room, providing an optical downlink. Power and data can be provided to each light fixture using a number of different techniques, including power over ethernet (PoE) and power line communication (PLC) [29,30]. An optical uplink is implemented by using a transmitter on the user equipment (UE), often using an IR source (so it is invisible to the user), and a receiver close to the light fixture. Each of these light fixtures, which at the same time act as wireless LiFi APs, create an extremely small cell (an attocell), which can provide high bandwidth density due to the highly confined illumination from an individual light source. The balance of light fixtures that contain APs and those that provide only illumination is determined by the requirement of the network, but potentially all light fixtures can contain APs. Compared to a single AP wireless hot-spot system, such cellular systems can cover a much larger area and allow multiple UEs to be connected simultaneously [31]. In cellular networks, dense spatial reuse of the wireless transmission resources is used to achieve very high data density - bits per second per square meter (bps/m^2). Consequently, the links using the same channel in adjacent cells interfere with each other, which is known as co-channel interference CCI [32]. Fig. 2 illustrates CCI in an optical attocell network.

Advanced CCI mitigation techniques often require that these multiple LiFi APs are operated by means of a centralised control mechanism [32] such as the 'hypervisor' within the server of a software defined network (SDN) [33]. The main tasks of the central controller are to adaptively allocate signal power, frequency, time and wavelength resources. Other functions of central controller include achieving multi-user, and the handover process from cell to cell when terminals move.

LAC networks have a number of advantages over incumbent technologies. Firstly, unlike omnidirectional RF antennas radiating signals in all directions, a LED light source typically radiates optical power directionally because of the way it is constructed. Therefore, the radiation of the visible light signals is naturally confined within a limited region. In contrast, RF mm-wave systems require complicated and expensive antenna beamforming techniques to achieve the same objective. Secondly, LAC networks can be implemented by
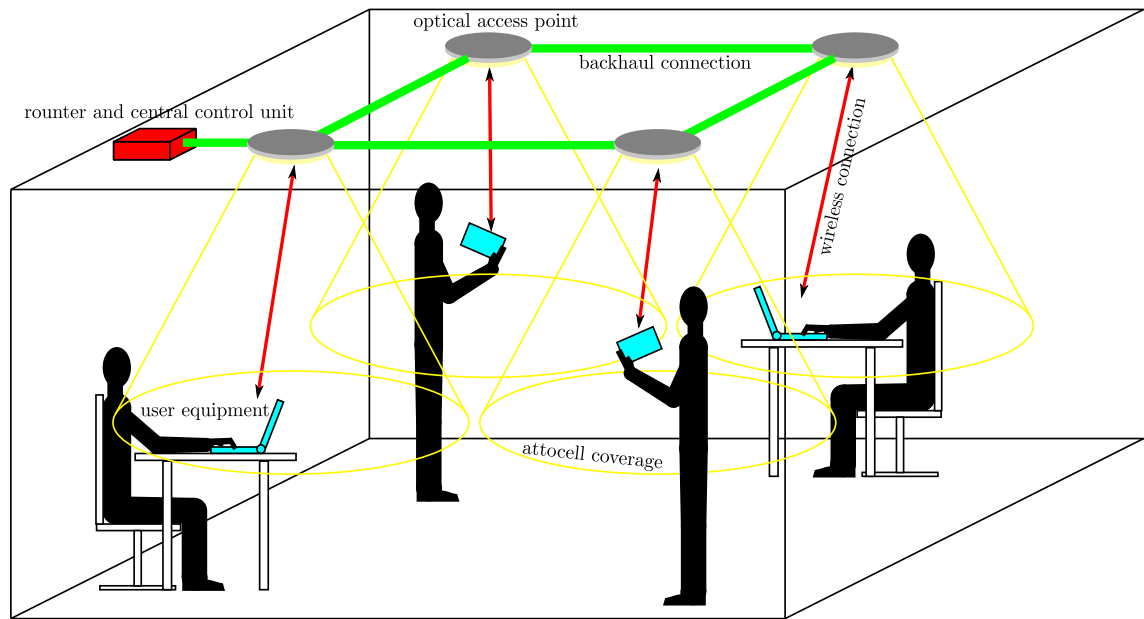
Fig. 1. Concept of LiFi attocell network. Lights in the ceiling act as optical access points forming a mobile network. A single optical access point can communicate to multiple terminals simultaneously in a bi-directional fashion. The system supports mobility. When a terminal leaves the coverage area of an optical access points and enters the coverage area of the neighboring access point a handover is initiated. This means service provision is seamless.

modifying existing lighting systems. Building a RF small-cell network with the same AP density imposes a huge infrastructure cost. In addition, any LAC network can provide extra capacity without interference to RF networks that may already exist. LAC networks, therefore, have the potential to augment 5th generation (5G) cellular systems in a cost-effective manner [34].

The move from point to point links to full wireless networks based on light poses several challenges. Within each cell, there can be a number of users and therefore multiple access schemes are required. Interference from signals used to communicate in adjacent cells must be considered and is likely to be the most significant impairment. The provision of an uplink (the communication link from a UE to one or more APs) can also require a different approach from the downlink. This is because low-energy consumption is required in the portable device, and an uplink visible light source on the device is likely to be distracting to the user. Each of these elements is discussed in the following sections.

2.1. Downlink and uplink transmission

In cellular systems, downlink communication is defined as the data transmission from an AP to a UE [32]. A basic setup for a LAC downlink system is shown in Fig. 3.

The illumination from the fixture is intensity modulated by the data and this propagates to a receiver on the UE. Typically, an optical
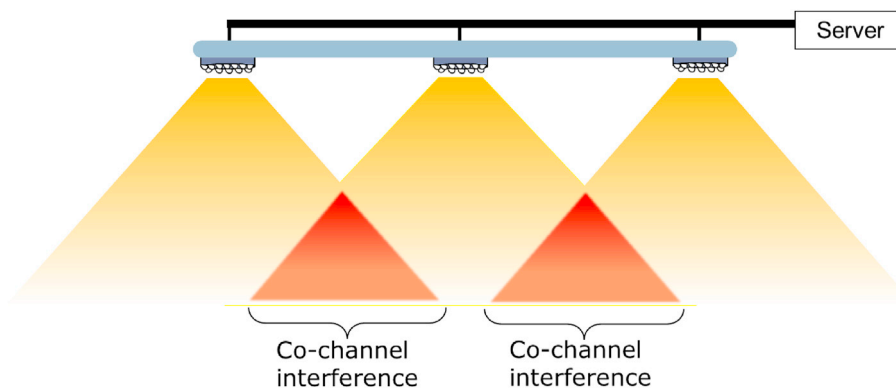

Fig. 2. CCI occurs in the region where the same light spectrum of neighbouring APs overlaps, and when these APs use the same modulation bandwidth for data encoding.
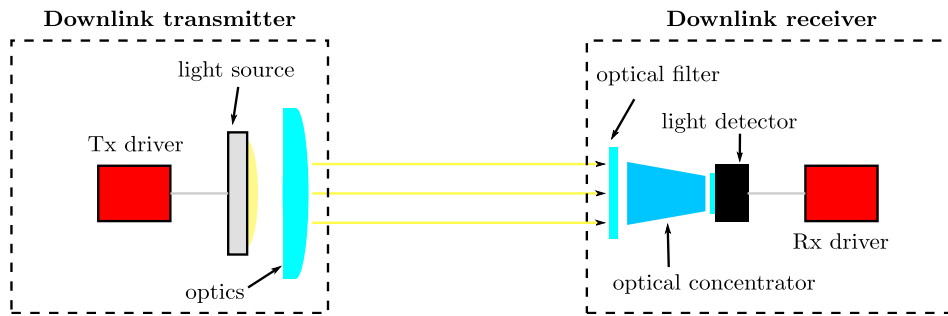
Fig. 3. Key components in a LAC downlink transmission system.

element is used to concentrate radiation onto a photodiode (PD) which then creates an electrical signal that is further amplified to recover the data. For the uplink IR links are usually preferred, as the wavelength separation between uplink and downlink allows simultaneous (full duplex) bi-directional communication with appropriate optical filtering. In addition, visible sources on the UE (usually a mobile device) are distracting. Another viable uplink solution is to use conventional RF transmission. Studies show that systems that only use VLC for the downlink and RF for the uplink show substantial efficiency gains over RF only networks [35].

2.2. Interference mitigation

The light radiation pattern of a visible light source with strong directionality confines most of the radiated optical power within the coverage area of an AP. Thus, CCI can primarily be expected at the cell boundaries, but due to overlapping light cones, CCI can be severe. Therefore, CCI poses major challenges to the downlink in LAC networks with dense spatial reuse.

Although this area of research is only in its infancy, there have been a number of studies. In Ref. [36], an interference coordination scheme based on busy-burst signalling has been proposed. Furthermore, angular diversity techniques have been considered for interference management [37]. In addition, fractional frequency reuse (FFR) and joint transmission (JT) in conjunction with angular diversity transmitter for LAC networks are investigated in Ref. [38].

2.3. Multiple access

In a cellular network, typically multiple UEs are located within the same cell. In this case, the AP must be able to serve multiple UEs at the same time, which is known as multiuser access (MA). A number of multiple access techniques have been developed in cellular systems such as time-division multiple access (TDMA), code-division multiple access (CDMA) [32,39,40], the more advanced orthogonal frequency division multiple access (OFDMA) [41], and non-orthogonal multiuser access (NOMA), which has gained significant attention recently [42,43].

A number of studies have been carried out to investigate MA in networked OWC systems [44,45]. In TDMA, each UE is given a particular time slot for transmission. This scheme can be directly used in an intensity modulation (IM)/direct detection (DD) based LAC system. In CDMA, the signal of each UE is 'encrypted' with a unique orthogonal code, which serves as a key, and all signals are transmitted at the same time and frequency channel. At the receiver, the desired signal is filtered out from the sum signal by using the respected key for that particular link. A number of designs of orthogonal codes are available to accommodate CDMA in a LAC network, such as optical orthogonal codes, unipolar *m*-sequences and Walsh-Hadamard codes. In an optical orthogonal frequency division multiplexing O-OFDM-based LAC system it, however, is more natural to use OFDMA by distributing different groups of orthogonal subcarriers to multiple UEs. In Ref. [45], it has been found that OFDMA out-performs CDMA in a multi-user VLC system. The unique features of VLC also enable wavelength-division multiple access (WDMA), if the corresponding transmitter is composed of multi-colour light sources [46]. In WDMA, different UEs are served by a unique, non-interfering wavelength.

2.4. Handover

Handover is defined as the process of transferring the management of an ongoing wireless transmission session from the current AP to another AP [47]. Handover is normally required in a case where a mobile terminal is moving out of the coverage area of an AP and is moving into the coverage area of an adjacent AP. In some cases, handover is also required if the transmission channel is severely degraded due to interference or if the current cell is fully loaded. A handover that stems from these two scenarios is usually classified as horizontal handover as it happens between APs in the same network [48]. However, typically there are multiple access technologies such as WiFi, LTE (long term evolution), and LiFi. This means that there are different types of access nodes in a heterogeneous network at different locations. If a UE is moving from indoor to outdoor where there might not be LiFi coverage, a seamless handover from LiFi to LTE will be triggered. This handover between APs of different systems is categorised as vertical handover [48]. A study of dynamic load-balancing schemes with handover in such hybrid system is presented in Ref. [49]. Generally, there are two types of handover schemes – hard handover and soft handover. In a hard handover process, the UE is disconnected from the current AP before it connects to the next

AP, which is simpler to implement and has lower hardware complexity [47]. However, the service could be interrupted with the hard handover scheme. In a soft handover process, the UE remains connected to the current AP until successful connection to the next AP is established. Soft handover offers better user experience, but requires more wireless transmission resources. With decreasing cell sizes, the handover frequency is expected to increase. Increased number of handover sessions causes losses in system throughput and a degraded quality of service. In a LAC network, handover overhead is particularly critical as LAC networks are constructed with the smallest cells in a cellular network. Since the handover frequency is expected to be high, soft handover may be preferred for better quality of service. Novel handover decision algorithms for LAC networks are required which also avoid ping-pong effects [48]. This is an area of very little research, and significant contributions can be expected in the future.

2.5. Backhaul connections

Backhaul is defined as the communication link between APs and the network controller [50]. Generally, backhaul connections should be able to provide reliable, high capacity and low latency transmission to carry the entire wireless access traffic from all APs. If high speed access networks are densely deployed in the future, the requirement of backhaul capacity will increase significantly [51]. A straightforward solution to the backhaul issue is to increase the deployment of optical fibre, which offers the best performance, but at very high cost. Cost-effective backhaul based on power over ethernet (PoE) and power-line communication (PLC) have also been considered [29,30]. In addition, a number of wireless backhaul solutions have been proposed such as mm-wave, microwave and free-space optical communication (FSO) [50,52,53].

The LiFi network is constructed from individual optical links. In the following sections, progress on the transmitter and receiver components, and details of the communications channel are described.

3. Point-to-point link level systems

3.1. Transmitter

Visible light is typically generated by a white LED, or a combination of red green and blue (RGB) LED emitters. Low cost white LEDs use a blue Gallium Nitride (GaN) emitter that excites a yellow inorganic phosphor. Direct blue emission from the GaN device combines with the broad yellow emission to create white light. Although the modulation bandwidth of white LEDs far exceeds that of traditional lighting sources, the large capacitance of the large area emitters and the slow response of the yellow phosphor limit the 3-dB bandwidth of white LEDs to a few MHz [54]. By removing the signal emitted from this yellow phosphor at the receiver side, the 3-dB modulation bandwidth can be increased to the range of 10–20 MHz.

LEDs designed for lighting are relatively robust and can be driven by a voltage source with the addition of some resistance to limit the driving current. A bias-T is often used to combine the alternating current (AC) data modulation with a direct current (DC) bias that creates the desired illumination level and ensures that the LED is always driven with a net positive signal. There have also been investigations into improving the emitter bandwidth by modification of the driving circuitry. Analogue pre-equalisation and fast LED driver circuits as well as resonant equalisation [55] have also been investigated. The LED device bandwidth can be altered by the use of different structures, notably by decreasing the size of the LED. Micro-LEDs, with active areas much smaller than those used in LED lamps, can show bandwidths of several hundred MHz, whilst emitting mW of optical power. A series of investigations has been undertaken [56–59], with the fastest reported data rates for such single LEDs exceeding 8 Gbps [60] which was only limited by the receiver. If this limitation can be overcome, it was shown in Ref. [60] that a single GaN micro LED is capable of transmitting at speeds of 11 Gbps.

The colour conversion phosphors used in commercial devices are not optimised for bandwidth. There has been work on a number of fast colour converting materials, including using organic [61], semiconductor [62], and perovskite materials [63]. The tradeoff between efficiency of conversion and speed, and the effect on overall device efficiency has yet to be investigated fully.

Whilst LEDs will provide a great majority of general lighting, there is increasing interest in laser based lighting and sources [64,65]. Extremely high brightness sources can be created for headlights and projection displays using a laser and a small phosphor target that is illuminated by performs colour conversion [66]. Sources of white light have also been demonstrated using phosphor plates and lasers [67,68] and Perovskite colour converters [63]. The use of RGB LED or laser sources offers the possibility of independent modulation of each of the LEDs, offering the possibility of increasing data rates substantially, albeit at increased cost and complexity, and a number of high rate demonstrations have been reported [65,69–71].

Most commercial lighting LEDs consist of multiple chips that are arranged in series or in parallel to create a single emitter with a higher output power. Optical elements are then used to capture as much of the wide-angle emission from the LED and direct it into the desired illumination pattern. LEDs must satisfy the indoor illumination standard and photobiological safety standard [72,73]. With increased emission powers, diffusing elements are often incorporated in order to achieve this. The light emission from a LED can be modelled by a radiation pattern defined by a generalized Lambertian law [7]. Relative to a given source location and orientation, the received optical power with a radiant angle of ϕ and a radiant solid angle Ω can be calculated as follows [7]:

$$P_{\text{opt},\Omega} = \Omega P_{\text{opt}} \frac{(m+1)}{2\pi} \cos^m \phi, \tag{1}$$

where P_{opt} is the total optical output of the LED source, and m denotes the Lambertian emission order, which is determined by the half-

power semi-angle by $m = -1/\log_2\left(\cos\left[\phi_{1/2}\right]\right)$.

The level of illumination required in the coverage area is determined by the needs of the user. According to [72], the required average illuminance in the task area[1] for working purposes, typically 0.75 m above the floor, should not be less than 500 lux. Illuminance is defined as the incident luminous flux per unit area [74], and is denoted as E_v. The power required from a single lamp to achieve this can be estimated, assuming Lambertian emission, and that the peak illuminance is directly below the lamp and matches that specified in Ref. [72]. Firstly, the luminous output flux of the source can be calculated by $\Phi_v = P_{opt}K_{e/v}$, where $K_{e/v}$ denotes the luminous efficacy which can be calculated as follows [74]:

$$K_{e/v} = \frac{683\int V(\lambda)\tilde{P}_{opt}(\lambda)\mathrm{d}\lambda}{\int \tilde{P}_{opt}(\lambda)\mathrm{d}\lambda}, \tag{2}$$

where $V(\lambda)$ is the luminosity function against wavelength λ; and $\tilde{P}_{opt}(\lambda)$ is the spectral radiant power density function of the lamp. With a given luminous output flux Φ_v, the emitted luminous flux to a solid angle of Ω can be calculated based on (1) as follows:

$$\Phi_{v,\Omega} = \Omega\Phi_v\frac{(m+1)}{2\pi}\cos^m(\phi). \tag{3}$$

The illuminance right below the luminaire with a distance of z can be calculated as:

$$\tilde{E}_v = \frac{A_r}{z^2}\Phi_v\frac{(m+1)}{2\pi A_r}[\cos(0)]^{m+1} = \frac{(m+1)\Phi_v}{2\pi z^2}, \tag{4}$$

where z is the vertical separation between light source and the height of the task area, and A_r is the physical area of the receiving element. Therefore, the average optical radiant output power should be:

$$\overline{P}_{opt} = \frac{\Phi_v}{K_{e/v}} = \frac{2\pi\tilde{E}_v z^2}{(m+1)K_{e/v}}. \tag{5}$$

Considering a room height of 3 m, with a $\phi_{1/2}$ of 20° to 45°, the required luminous flux for a minimum illuminance of 500 lux is in the range of 1300 lumen–5300 lumen. This amount of power agrees with the specification of commercially available LED downlighters and LED panels for lighting in offices and public areas [75,76]. This high optical power output of the LED sources ensures sufficient signal strength for reliable communication. Note that the rated power of a LED lamp for residential home is typically lower than this level (< 1000 lumen), where lower levels of light are generally preferred.

3.2. Receiver

The right hand side of Fig. 3 shows a typical receiver. Light is received and concentrated onto a PD using an optical element. The PD then converts this to an electrical signal which is pre-amplified and then fed to data recovery and signal processing. In some cases, an optical filter is used to restrict the spectrum of light that is fed to the receiver. The bandwidth, sensitivity and area of the detector/preamplifier pair determine the overall performance of the receiver, and ultimately the quality of the communication channel. A small detector is desirable as it can have low capacitance and high bandwidth, but a doubling of the detector area increases the power received by the same factor, and is equivalent to an increase in sensitivity. Therefore, it is not straightforward to determine the optimum receiver design. Each element in the receiver is described below.

3.2.1. Optical filter and concentrator

An optical filter can be used to cut-out IR and other ambient light sources as well as blocking the slow light from the yellow phosphor colour conversion from commercial LEDs. Analysis of the effect of this blue filtering was undertaken as an example in Ref. [77], showing that modest gains in performance can be achieved. Optical concentrators ideally receive light from a wide field of view (FoV) and concentrate it onto a small PD. However, such devices are etendue limited [78], so that the product of collection area and FoV is a constant. The performance of the system is therefore limited by the PD area, as its FoV is generally 2π steradians. The geometric gain of an optical concentrator is defined as [78]:

$$G_c = \frac{\mathfrak{n}^2}{\sin^2\psi_{FoV}}1_{\psi \leq \psi_{FoV}}(\psi) \tag{6}$$

where $\mathfrak{n}$ denotes the internal refractive index, ψ is the incident angle to the receiver, and ψ_{FoV} is the FoV of the receiver. The indicator function $1_D(u)$ is defined as:

$$1_D(u) = \begin{cases} 1 & : u \in D \\ 0 & : u \notin D \end{cases}. \tag{7}$$

Compound parabolic concentrators [78], or more modern designs [79] show concentration ratios around 50% of the etendue limit.

---

[1] The area where illumination is required [72].

However, recent work shows that designs based on fluorescent slab solar concentrators [80] show measured gains that exceed the etendue limit [81], with predictions of gains far exceeding these early results [80].

3.2.2. Photodetector and preamplifier

The combination of PD and preamplifier set the sensitivity of the receiver and its bandwidth, and the design of low noise receivers is beyond the scope of this paper (see Ref. [82] for a comprehensive description). In free-space applications, the capacitance of the PD becomes significant as large areas are required to collect as much light as possible. The ideal preamplifier would therefore offer high bandwidth and be tolerant to high input capacitance. These issues have been addressed in some designs for IR applications (for example [83–85]), and in VLC the high dynamic range requirements must also be considered. Both PIN and avalanche photodiode (APD) structures have been used for VLC experiments with APDs providing greater sensitivity (typically 10 dB) than their PIN counterparts. The choice of detector involves the area, capacitance, any transit-time limited bandwidth effects, and the spectral response. As most of the useful signal is carried in the blue emission, the increased sensitivity in this region is favoured. However, the high levels of signal present offer good performance with a wider range of relatively low-performance receiver designs, so this has not been an area where there has been significant effort. Integration of detectors and amplifiers within complementary metal oxide semiconductor (CMOS) circuits is an area of growing interest, with designs using linear-mode APDs [86] and PIN sructures have been reported [87].

As well as APDs used as conventional detectors, single photon avalanche detectors (SPADs) have also been used for VLC, using both pulse based [88] and OFDM [89] modulation schemes. SPADs are photon counting detectors and have the potential to yield improvements in sensitivies of an order of magnitude over linear APDs (for similar detection areas). However, at present, difficulties with the dead time, fill-factor and dark-noise of these devices means that they have yielded only limited gains [90].

3.3. The optical wireless channel

The communications channel consists of the path taken from the electrical signal that modulates the data onto the transmitter to the electrical signal at the receiver. The quality of the received signal is measured by the signal to noise ratio (SNR) for a single channel. In the case of a network, the signal to interference-plus-noise ratio (SINR) is used to characterise the communication link. The bandwidth and path loss of the channel are key metrics in determining overall system performance, and techniques to estimate them are described in the following sections.

3.3.1. Bandwidth

The front-end elements of a VLC system introduce low-pass responses. In addition, due to the reflective indoor environment, the receivers collect signals stemming from multiple paths, and this results in a frequency-selective transfer characteristic. The combined channel is equivalent to a number of filters connected in series. The optical transmitter front-end, the optical receiver front-end, free-space signal propagation, can all be modelled as independent filters. Here the properties of combined channel can be characterised by its impulse response as follows:

$$h(t) = h_{\mathrm{fe}}(t) \otimes h_{\mathrm{fs}}(t), \tag{8}$$

where $h_{\mathrm{fs}}(t)$ denotes the channel impulse response (CIR) due to the free-space light propagation in the considered indoor environment, $\otimes$ denotes mathematical convolution, and $h_{\mathrm{fe}}(t)$ denotes the CIR due to the effects of front-end elements. With the knowledge of the CIR $h(t)$, the corresponding frequency response can be calculated by using the Fourier transform:

$$H(f) = \int_0^{\infty} h(t) \exp(-j2\pi ft) \mathrm{d}t = H_{\mathrm{fe}}(f) H_{\mathrm{fs}}(f). \tag{9}$$

3.3.2. Transmitter and receiver response

The net-effects of the transmitter and receiver lead to a system with low-pass characteristic which is considered in this subsection. The front-end low-pass characteristic can be estimated from a number of experimental studies [22,91–93]. Fig. 4 shows the normalised channel gains against frequency, f, in the aforementioned experimental results. The 3-dB bandwidth of these systems are in the range from 10 MHz to 60 MHz. As many VLC systems operate at data rates many times greater than the 3-dB bandwidth, due to the high available SNR, a model of the rate at which the channel rolls off is useful in determining overall performance. The exact response and rate of roll-off with frequency is difficult to measure and model. For the LEDs, bandwidth is current density dependent, so as current levels vary the bandwidth changes dynamically. At the receiver, simple first order response is usually a reasonable approximation, but for large area detectors with high bias transit time limitations can alter this [94].

A suitable simple model is to approximate the normalised channel gain, due to the effects of the front-end elements, with respect to frequency [91]:

$$\left| H_{\mathrm{fe}}(f) \right|^2 = \exp\left(-\frac{f}{F_{\mathrm{fe}}} \right), \tag{10}$$

where F_{fe} controls the frequency characteristics of the front-end elements. The higher the value of F_{fe}, the wider the modulation bandwidth. As shown in Fig. 4, this approximation closely follows the low-pass characteristics measured in the experiments.
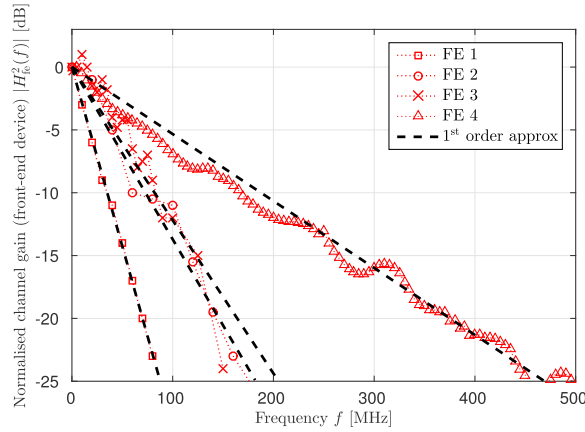
Fig. 4. Normalised channel gain due to the front-end device filtering. The channel gains of the FE1, FE2 and FE3 are presented in Refs. [91–93], respectively. Commercially available white LEDs are used in these systems. The channel gain of FE4 is an experimental measurement of the same system presented in Ref. [22] which uses a 50-μm GaN micro LED.

3.3.3. Indoor free-space propagation of light

In this subsection, the major components of the free-space propagation channel are introduced. Primarily, if there is no obstruction between the transmitter and the receiver, a LoS channel exists. Secondly, the channel is also composed of a non-line-of-sight (NLoS) part due to the reflections by room internal surfaces and other objects. For the convenience of characterising the LoS and NLoS parts, the basic principle of the channel DC gain from a source element to a receiving element is introduced first [95].

3.3.4. Channel DC gain

As shown in Fig. 5, an optical source, $\mathscr{S}$, with a location vector of $\vec{a}_s$, a direction vector of $\vec{o}_s$ is defined. In addition, a receiving element, $\mathscr{R}$, with a location vector of $\vec{a}_r$, a direction vector of $\vec{o}_r$, a FoV of ψ_{FoV} and a physical area of A_r is defined. Considering the source as origin, the emitted power within a certain solid angle will incident on to the receiving element. Since this solid angle is extremely small, it can be approximated as follows:

$$\Omega = \frac{A_r \cos(\psi)}{D^2} \quad [\text{sr}] \tag{11}$$

where D denotes the Euclidean distance between the $\mathscr{S}$ and $\mathscr{R}$. Since it is known that the emitted power with a solid angle of Ω and a radiant angle of ϕ at a source can be calculated by (1). Then the collected power by the receiving element, $\mathscr{R}$, can be determined as:
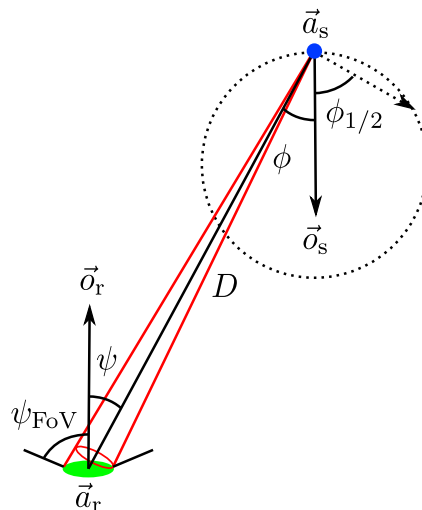

Fig. 5. Channel DC gain geometry.

$$H_{\mathrm{DC}} = \frac{(m+1)A_{\mathrm{r}}}{2\pi D^2}\cos^m(\phi)\ \cos(\psi)\ 1_{\psi \leq \psi_{\mathrm{FoV}}}(\psi). \tag{12}$$

where the quantities D, ϕ and ψ can be calculated as follows [96]:

$$D = ||\overrightarrow{a}_{\mathrm{s}} - \overrightarrow{a}_{\mathrm{r}}||, \tag{13}$$

$$\cos(\phi)\ = \overrightarrow{o}_{\mathrm{s}} \cdot (\overrightarrow{a}_{\mathrm{r}} - \overrightarrow{a}_{\mathrm{s}})/D, \tag{14}$$

$$\cos(\psi)\ = \overrightarrow{o}_{\mathrm{r}} \cdot (\overrightarrow{a}_{\mathrm{s}} - \overrightarrow{a}_{\mathrm{r}})/D. \tag{15}$$

where the operator $\cdot$ represents the dot product operation.

3.3.5. Line-of-sight channel impulse response

The setup for the LoS channel is illustrated in Fig. 6. The LoS CIR can be directly calculated based on (12) with a specified transmitter $\mathscr{S}_{\mathrm{Tx}}$ and receiver $\mathscr{R}_{\mathrm{Rx}}$ as follows:

$$h^{[0]}(t, \mathscr{S}_{\mathrm{Tx}}, \mathscr{R}_{\mathrm{Rx}}) = \frac{(m+1)}{2\pi D^2}A_{\mathrm{pd}}G_{\mathrm{f}}G_{\mathrm{c}}\cos^m(\phi)\cos(\psi)1_{\psi \leq \psi_{\mathrm{FoV}}}(\psi)\delta\left(t - \frac{D}{c}\right), \tag{16}$$

where $\delta(u)$ represents the Dirac delta function. Note that A_{r} in (12) equals the actual physical area of the PD, A_{pd}, in the LoS channel, and the resulting CIR is to be scaled by the optical filter loss G_{f} and optical concentrator gain G_{c} at the receiver side.

3.3.6. Diffused channel impulse response

A number of studies have been carried out to evaluate the NLoS channel due to the reflections by the indoor internal surfaces [96–100]. Generally, a cuboid room is defined with a certain size and internal surfaces with fixed reflectance, as shown in Fig. 6. Typical room internal surfaces such as plaster walls cause a diffused reflection. The specular reflections caused by mirrors or windows are considered as special cases. Here, we focus on the channel caused by diffused reflections. The NLoS channel introduced by human bodies and other objects are difficult to predict and model. Developing more comprehensive channel models, including these extra NLoS components, is subject to ongoing research. There are two popular methods based on ray-tracing techniques to calculate the NLoS CIR due to the internal surface reflections. The first approach uses a deterministic method to calculate the NLoS channel [96], while the other approach is based on a Monte Carlo method [97]. For the convenience of this description, these two methods are termed as deterministic method and Monte Carlo method, respectively.

3.3.7. Deterministic NLoS CIR calculation method

By using the deterministic method, the CIR is decomposed of multiple components due to different orders of reflections [96]:
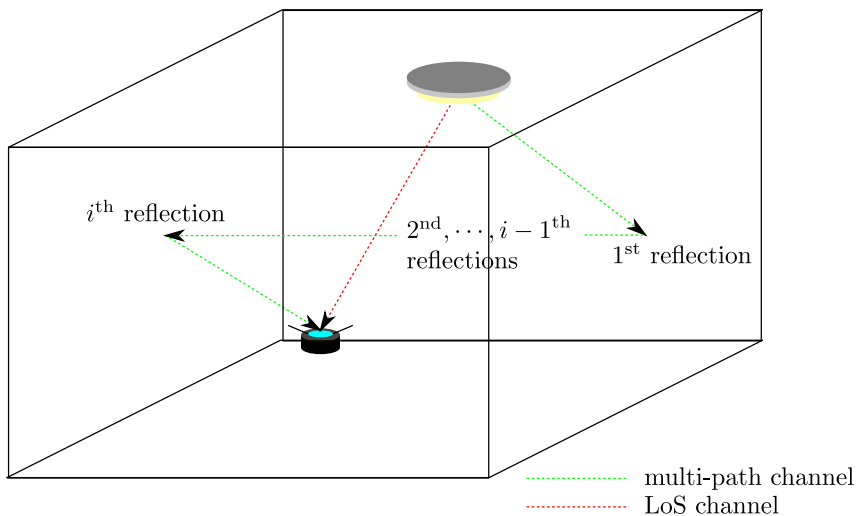

Fig. 6. Illustration of LoS propagation channel and NLoS multipath propagation channel.

$$h_{\text{fs}}(t, \mathscr{S}_{\text{Tx}}, \mathscr{R}_{\text{Rx}}) = \sum_{i=0}^{\infty} h^{[i]}(t, \mathscr{S}_{\text{Tx}}, \mathscr{R}_{\text{Rx}}), \tag{17}$$

where $h^{[i]}(t, \mathscr{S}, \mathscr{R})$ is the CIR from $\mathscr{S}$ to receiving element $\mathscr{R}$ undergoing exactly i reflections. In the case of $i = 0$, this refers to the LoS CIR. To accommodate the numerical evaluation of CIR, the entire internal surface is divide into N_e blocks. The location vector and orientation vector of each block are denoted as $\vec{a}_n$ and $\vec{o}_n$, respectively. These blocks operate in both transmitting mode and receiving mode in the considered NLoS channel. In the transmitting mode, the nth block is treated as a source element, $\mathscr{S}_n$, with a radiation mode number of 1. In the receiving mode, the nth block is treated as a receiving element, $\mathscr{R}_n$. The maximum incident angle can be as large as $\pi/2$ ($\psi_{\text{FoV}} = \pi/2$), and the receiving block has a physical area of ΔA. In addition, the received power should be scaled by the reflectivity of the block ρ_n. The CIR component experiencing i reflections can be calculated based on the CIR component experiencing $i - 1$ reflections as follows [96]:

$$h^{[i]}(t, \mathscr{S}_{\text{Tx}}, \mathscr{R}_{\text{Rx}}) = \sum_{n=1}^{N_e} h^{[0]}(t, \mathscr{S}_{\text{Tx}}, \mathscr{R}_n) \otimes h^{[i-1]}(t, \mathscr{S}_n, \mathscr{R}_{\text{Rx}})$$

$$= \frac{m+1}{2\pi} \sum_{n=1}^{N_e} \frac{\rho_n \cos^m(\phi_n)\cos(\psi_n)}{D_n^2} 1_{\psi_n \leq \pi/2}(\psi) h^{[i-1]}\left(t - \frac{D_n}{c}, \{\vec{a}_n, \vec{o}_n, 1\}, \mathscr{R}_{\text{Rx}}\right) \Delta A, \tag{18}$$

where D_n, ϕ_n and ψ_n refer to the quantities between $\mathscr{S}_{\text{Tx}}$ and $\mathscr{R}_n$. The accuracy of this method increases as N_e increases or equivalently ΔA decreases. However, the calculation of an accurate CIR result requires high computational complexity, thereby taking a very long time to generate a single CIR.

3.3.8. Monte Carlo NLoS CIR calculation method

In the Monte Carlo method, a random propagation path is traced in each Monte Carlo iteration [97]. By repeating the tracing process a significant number of times, a stable CIR result can be generated. The Monte Carlo method is summarised in Algorithm 1.

Algorithm 1 : CIR simulation with Monte Carlo method

1: Initialise $P_{\text{opt},h}(t) = 0$ for all $t \in (0, t_{\text{max}})$.

2: **for** $n_{\text{iter}} = 1, 2, \cdots, N_{\text{iter}}$ **do**

3:    Start to trace a photon with a unity power and a random direction, $\hat{\tau} = 0, \hat{P}_{\text{opt}} = 1$

4:    **while** $\hat{\tau} < t_{\text{max}}$ **do**

5:       Propagate the photon until it reach any obstacle with a travelling distance of D, $\hat{\tau} = \hat{\tau} + \frac{D}{c}$.

6:       Attenuate the power of the photon with the reflectance of the surface, $\hat{P}_{\text{opt}} = \rho \hat{P}_{\text{opt}}$.

7:       Calculate the CIR contribution to the receiver using (19).

8:       Generate a new direction for the following propagation of the photon.

9:    **end while**

10: **end for**

11: Normalise the result CIR with N_{iter} as $h_{\text{fs}}(t) = P_{\text{opt},h}(t)/N_{\text{iter}}$.

In step 1 of Algorithm 1, an empty vector $P_{\text{opt},h}(t)$ recording the received optical power at time instant t is initialised with a maximum delay of t_{max}. In step 3, $\hat{P}_{\text{opt}}$ is defined to record the optical power loss in the propagation, and it is initialised with a value of $\hat{P}_{\text{opt}} = 1$. $\hat{\tau}$ is defined to record the time that the ray has experienced, and it is initialised with a value of zero. As long as the transmission time has not reached t_{max}, the propagation continues. For each transmission from one point to another, the propagation distance D is calculated. Based on D, the experienced transmission time $\hat{\tau}$ can be updated. In addition, the output power for the next propagation will be attenuated by the reflectivity of the contacted surface ρ. Furthermore, the power contribution to the CIR optical power vector from the current point is updated using (19). For the next propagation, a new random direction should be generated. In step 3 and step 8 of

Algorithm 1, the probability of each possible direction is proportional to the radiation intensity along that direction. With a large number of iterations of the same tracing process for N_{iter} times, the final CIR can be calculated by normalising $P_{opt,h}(t)$ with the number of iterations N_{iter}. The details of the Monte Carlo method are provided in Ref. [97]. As long as N_{iter} is large enough, an accurate CIR with low noise can be obtained. This method requires less computational complexity. However, due to the randomness in the calculation, minor simulation errors are inevitable.

$$P_{opt,h}\left(\widehat{\tau}\right) = P_{opt,h}\left(\widehat{\tau}\right) + \frac{\widehat{P}_{opt}A_{pd}}{\pi D^2}1_{\psi \leq \pi/2}(\psi)\cos(\phi)\ \cos(\psi). \tag{19}$$

3.3.9. Overall channel response

Modelling of the effects of the transmitter, receiver and propagation lead to a normalised frequency response where the transmitter limits the overall bandwidth, and the rate of roll-off of the response has contributions from the transmitter, receiver and propagation. The absolute level of received signal is set by the transmitter power, which is set by the level of illumination required within the space, and the degree to which this power is modulated for communications. As described earlier, the required average illuminance in the task area for working purposes, typically 0.75 m above the floor, should not be less than 500 lux. This leads to extremely high signal to noise ratios at the receiver (see Fig. 18) for reference). Fig. 7 shows a measured channel gain for a LoS channel. In this case, the range of usable SNR is $\approx$ 50 dB, with a frequency range of several hundred MHz, despite a 3 dB bandwidth of several MHz. Such responses are typical, and show that the channel can be characterised as high SNR, low bandwidth. Optimising the use of this channel resource has led to work on multichannel communications, so-called optical multiple-input multiple-output (MIMO) [101,102] and spatial modulation [103], where individual transmitters send different data streams to multichannel receivers. Efficient multilevel modulation schemes which allow full use of the available SNR over a wide frequency range. An overview of each is given below.

3.4. Modulation

The simplest means of transmitting data is by using a pulse based scheme such as on-off keying (OOK), where a binary 'one' is represented as a pulse, and a binary 'zero' by the absence of a pulse. However, this does not make efficient use of the SNR that is available across a wide frequency range. Multi-level modulation schemes enable this. An additional improvement can be achieved by using multi-channel transmission such as OFDM, which is the most widely used example. This is because in OFDM each orthogonal sub-channel can be treated independently and with optimum bit loading and power loading it is possible to closely reach the maximum available channel capacity [104,105]. OFDM uses the fast Fourier transform (FFT) to multiplex several parallel channels. There are very computational efficient implementations of FFT which renders OFDM a very attractive technique from a practical perspective. However, alternative multi-carrier techniques have been proposed [106] based on other orthogonal transformations such as the Walsh-Hadamard transform [107]. A second class of methods comprise of single-carrier modulation with equalisation [108], carrier-less amplitude and phase (CAP) schemes [16] and pulse amplitude modulation (PAM) schemes [109]. These have found favour in optical fibre transmission using visible light where the simple implementation is particularly attractive.

3.5. O-OFDM transmission

As eluded to in Section 2.1, to ensure the high spectral efficiency in the downlink of a LAC network, O-OFDM modulation is the most attractive method. In this subsection, the downlink transmission using O-OFDM is analysed on a link level. Fig. 8 illustrates the key
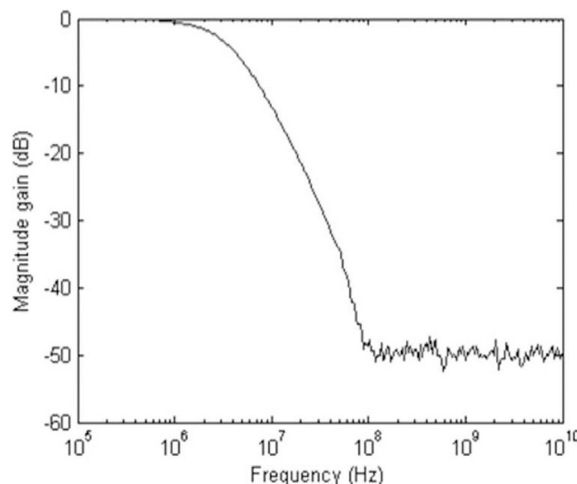

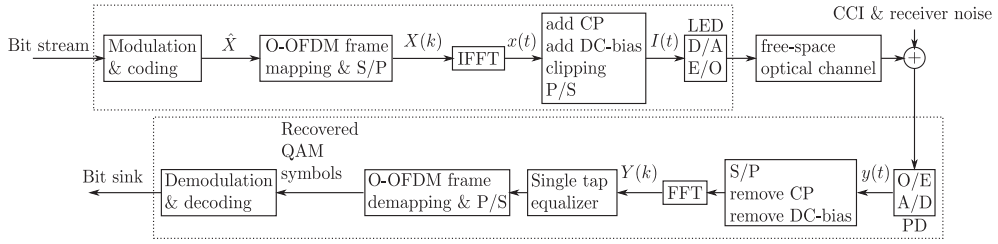**Fig. 7.** Typical measured channel gain.

Fig. 8. O-OFDM transmission block diagram: S/P refers to series-to-parallel conversion, P/S refers to parallel-to-serial conversion, D/A refers to digital-to-analogue conversion, A/D refers to analogue-to-digital conversion, E/O refers to electrical-to-optical conversion, and O/E refers to optical-to-electrical conversion.

elements of an O-OFDM communication system.

At the beginning of the transmission, the bit stream is coded and mapped to quadrature amplitude modulation (QAM) symbols $\widehat{X}$ with unity average symbol energy. Then, the $\tilde{K}$ QAM symbols are grouped and converted to a block of symbols which forms an OFDM frame $\overrightarrow{X}$ as [110]:

$$\overrightarrow{X} = [X(0), X(1), \cdots, X(K-1)], \tag{20}$$

where $X(k)$ is the kth QAM symbol in the OFDM frame $\overrightarrow{X}$. The electrical to optical conversion is carried out in time domain. The time domain signal strength associated with a specified light source configuration is important. Therefore, the time-domain OFDM symbol should be normalised. In order to ensure that the time-domain OFDM symbol have unity power after inverse fast Fourier transform (IFFT) operation, each QAM symbol is amplified by a factor of ξ as $X = \xi\widehat{X}$ [111]. The value of the amplification coefficient ξ can be determined by the following relationship:

$$\frac{\xi^2}{K} \sum_{k=0}^{K-1} \widehat{X}^2(k) = 1. \tag{21}$$

In an IM/DD-based O-OFDM system, the time-domain signal has to be real and positive. Consequently, in the formation of the OFDM frame, Hermitian symmetry must be applied: $X(0) = X\left(\frac{K}{2}\right) = 0$ and $X(K-k) = X^*(k)$ for $k = 1, 2, \cdots, \frac{K}{2}-1$, where $[\cdot]^*$ denotes the complex conjugate operation. An example of OFDM signal conversion with Hermitian symmetry is illustrated in Fig. 9.

There are two types of basic O-OFDM schemes, direct-current-biased optical (DCO)-OFDM [112] and asymmetrically clipped optical (ACO)-OFDM [113]. DCO-OFDM and ACO-OFDM use different frame structures and methods to avoid negative samples in time-domain. In DCO-OFDM, $\tilde{K} = \frac{K}{2}-1$ symbols are mapped to $\overrightarrow{X}$ with $k = 1, 2, \cdots, \tilde{K}$. Thus, there is a scaling factor $\xi = \sqrt{K/(K-2)}$ required. In ACO-OFDM, $\tilde{K} = \frac{K}{4}$ symbols are mapped to $\overrightarrow{X}$ with odd subcarriers ($k = 1, 3, 5, \cdots, \tilde{K}$). This leads to $\xi = \sqrt{2}$. All QAM symbols in the OFDM frame are mapped to unique orthogonal subcarriers. This operation can simply be realised by a *K*-point IFFT operation:

$$x(t) = \frac{1}{\sqrt{K}} \sum_{k=0}^{K-1} X(k) \exp\left(\frac{j2\pi kt}{K}\right). \tag{22}$$

By means of this operation, the bi-polar discrete time-domain OFDM signal can be obtained. Next, a cyclic-prefix (CP) is added to the start of every *K*-samples of the discrete time-domain OFDM signal, which allows the impairment of inter-symbol interference (ISI) to be removed by a single-tap equalisation at the receiver. Before the conversion of the electrical signal to an optical signal, the bi-polar time-domain signal should be converted to a unipolar signal with limited amplitude range via clipping and biasing. This process can be described by:
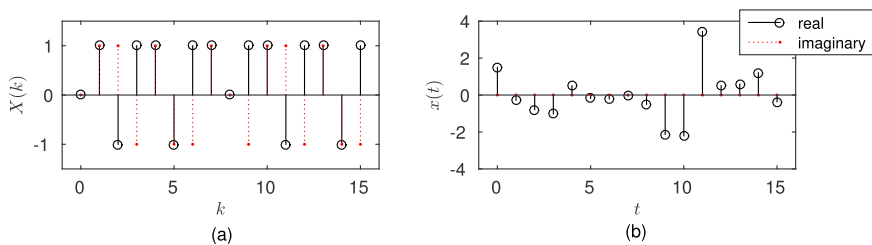

Fig. 9. An example of OFDM signal conversion from frequency domain to time domain with Hermitian symmetry. (a) Frequency-domain OFDM frame with QAM symbols before IFFT. (b) Time-domain OFDM signal after IFFT.
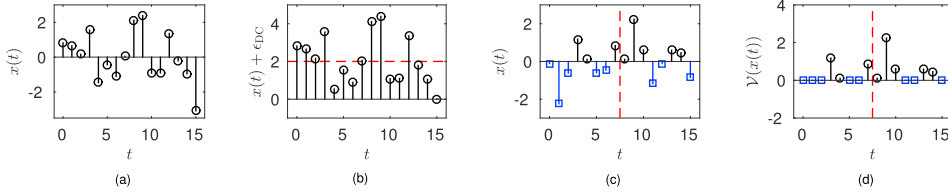
Fig. 10. Illustration of unipolar signal conversion in DCO-OFDM and ACO-OFDM. (a) Time-domain OFDM signal after IFFT operation in DCO-OFDM. (b) Time-domain OFDM signal with DC-bias in DCO-OFDM. (c) Time-domain OFDM signal after IFFT operation in ACO-OFDM. (d) Time-domain OFDM signal with negative samples clipped in ACO-OFDM.

$$I(t) = \sigma_{\mathrm{x}}(\mathscr{V}(x(t)) + \varepsilon_{\mathrm{DC}}), \tag{23}$$

where $\varepsilon_{\mathrm{DC}}$ denotes a normalised DC-bias level, σ_{x} denotes a signal amplification factor that makes the forward current fit the dynamic range of the LED front-end element, and $\mathscr{V}(u)$ represents the signal clipping function which is defined as:

$$\mathscr{V}(u) = \begin{cases} \varepsilon_{\max} & : u \geq \varepsilon_{\max} \\ u & : \varepsilon_{\max} > u > \varepsilon_{\min} , \\ \varepsilon_{\min} & : u \leq \varepsilon_{\min} \end{cases} \tag{24}$$

where $\varepsilon_{\max}$ and $\varepsilon_{\min}$ are the normalised top and bottom clipping levels, respectively [111]. The realisation of a unipolar signal is achieved differently in the two considered O-OFDM schemes. An example of the bi-polar discrete time-domain signal after the IFFT in DCO-OFDM is shown in Fig. 10 (a). The basic concept of DCO-OFDM is to add a positive DC-bias to turn the majority of the negative samples positive as shown in Fig. 10 (b), and the remaining negative samples are clipped to zero. Therefore, in DCO-OFDM, $\varepsilon_{\mathrm{DC}}$ is configured with a positive value. An example of the bi-polar discrete time-domain signal after the IFFT in ACO-OFDM is shown in Fig. 10 (c). The figure shows that the first half of the samples are the same as the second half multiplied by the signum function: $(x(t+K/2) = -x(t))$. Therefore, after the clipping of all negative samples (Fig. 10 (d)), the information of all samples can be recovered based on this relationship. With a linear dynamic range of $[0, I_{\max}]$, the DC-bias is zero in ACO-OFDM ($\varepsilon_{\mathrm{DC}} = 0$). Then the electrical signal with unity power is amplified by a factor of σ_{x} and converted to an optical signal by the LED front-end element. The output optical signal can be calculated as: $P_{\mathrm{opt}}(t) = \eta_{\mathrm{led}}I(t)$.

According to the Bussgang theorem, the non-linear clipped signal can be modelled as follows [111]:

$$\mathscr{V}(x(t)) = \eta_{\mathrm{clip}}x(t) + n_{\mathrm{clip}}(t), \tag{25}$$

where η_{clip} is a signal attenuation factor due to the clipping operation and $n_{\mathrm{clip}}(t)$ is the time-domain clipping noise sample.

3.5.1. Nonlinear impairments

The random time-domain OFDM waveform amplitude closely follows a Gaussian probability density function (PDF) if the system is designed to have more than about 64 sub-carriers. The system requires a linear channel response with a large dynamic range to be transmitted without causing non-linear distortions [111]. However, a typical LED has a quasi-linear response over a limited range, so
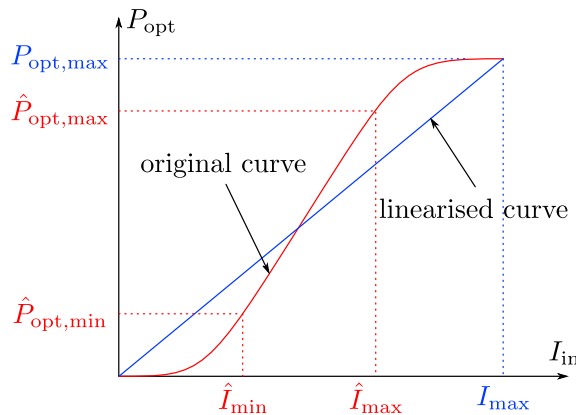

Fig. 11. A typical relationship between driving current and output optical power of a LED. The red curve shows a typical non-linear relationship between the driving current and the optical output power. The blue curve shows an ideal linearised conversion after pre-distortion. (For interpretation of the references to colour in this figure legend, the reader is referred to the web version of this article.)

both the dynamic range and the linearity within the range need to be considered. A typical response of a LED is shown in Fig. 11. In order to maximise the electrical signal power output per unit optical output, pre-distortion techniques can be used [114,115]. It has been shown that by using pre-distortion, an almost idealised linear relationship between input current and optical output can be established [116]. Consequently, the optical power can be modelled as follows:

$$P_{opt} = \begin{cases} \eta_{led} I & : 0 \leq I \leq I_{max} \\ P_{opt,max} & : I > I_{max} \end{cases}, \tag{26}$$

where I denotes the input current to the LED, and η_{led} denotes the conversion coefficient from the input current to the optical output power, which includes the electrical signal amplification and the LED quantum efficiency. An idealised linear relationship between input current and output optical power is assumed on the condition that $I \leq I_{max}$. The optical output power is saturated at a fixed level of $P_{opt,max}$ on the condition that $I > I_{max}$. Therefore, in order to avoid saturation, the input current has to fulfil $0 \leq I(t) \leq I_{max}$, where $I(t)$ represents the instantaneous input current at time instant t. Thus, the relationship between the input current and the average optical output power can be modelled as follows:

$$\overline{P}_{opt} = \eta_{led} \mathbb{E}_t[I(t)]. \tag{27}$$

The electrical signal power conveyed in the light wave can be estimated based on (27) with a specified dynamic range of the LED and a specified signal clipping used in O-OFDM.

The required dynamic range of the O-OFDM signal is characterised by the peak-to-average power ratio (PAPR). In order to ensure that the peak power stays within the dynamic range, a significant power back-off and a signal clipping would need to be applied, which causes a considerable reduction in the SNR level. There is a trade-off between power back-off and clipping level. On the one hand, with too much power back-off, the signal strength would not be enough to overcome the receiver noise distortion. On the other hand, too much signal clipping would lead to a serious non-linear distortion. This means that there is an optimum power back-off and clipping configuration which has been described in Ref. [111]. As shown in Fig. 12, a top clipping level ε_{max}, a bottom clipping level ε_{min} and a DC-bias level ε_{DC} are defined. The configuration of these parameters should fulfil the following relationship [111]:

$$\sigma_x(\varepsilon_{DC} + \varepsilon_{max}) = I_{max}, \tag{28}$$

$$\sigma_x(\varepsilon_{DC} + \varepsilon_{min}) = I_{min}, \tag{29}$$

where I_{max} and I_{min} denote the maximum and minimum forward current for the LED. The assumptions are that $I_{min} = 0$ leads to $\varepsilon_{min} = -\varepsilon_{DC}$ and $\varepsilon_{max} = \frac{I_{max}}{\sigma_x} - \varepsilon_{DC}$. Clipping at several standard deviations from the mean of the Gaussian distributed information signal is widely used. A number of studies have been carried out to investigate the effects of this clipping process [111,117].

3.5.2. Clipping distortion

As introduced in Section 3.5, the time-domain clipped signal can be modelled by (25). The attenuation factor can be derived as [117]:

$$\eta_{clip} = \mathbb{E}[x(t) \mathcal{V}'(x(t))] = \int_{-\infty}^{\infty} x(t) \mathcal{V}'(x(t)) f_{\mathcal{N}}(x(t)) dx(t) = \mathcal{Q}(\varepsilon_{min}) - \mathcal{Q}(\varepsilon_{max}). \tag{30}$$

where $\mathcal{Q}(u) = \frac{1}{\sqrt{2\pi}} \int_u^{\infty} \exp\left(-\frac{v^2}{2}\right) dv$ represents the Q-function; and $f_{\mathcal{N}}(u) = \frac{1}{\sqrt{2\pi}} \exp\left(-\frac{u^2}{2}\right)$ is the probability density function (PDF) of the standard normal distribution

The clipping noise variance in the frequency domain can be determined as follows [117]:

$$\sigma_{clip}^2 = \mathbb{E}\left[n_{clip}^2(t)\right] - \mathbb{E}^2\left[n_{clip}(t)\right] \tag{31}$$

where $\mathbb{E}[n_{clip}^2(t)] = \mathbb{E}[\mathcal{V}^2(x(t))] - \eta_{clip}^2 \mathbb{E}[x^2(t)]$ and $\mathbb{E}[n_{clip}(t)] = \mathbb{E}[\mathcal{V}(x(t))]$. With further equation expansion, the clipping noise variance can be written as:
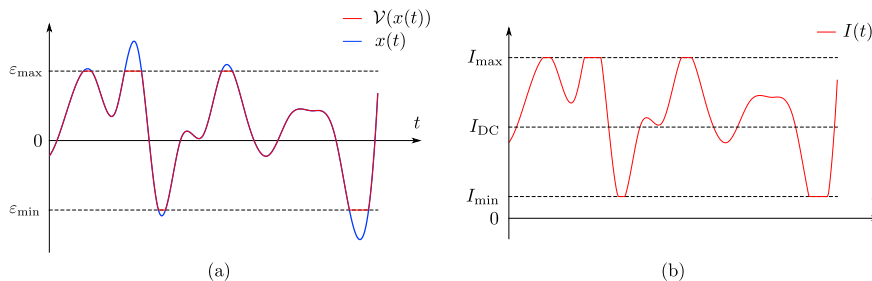

Fig. 12. (a) A clipped bi-polar signal with unity power. (b) A clipped signal after the addition of DC-bias and signal amplification to match the LED dynamic range.
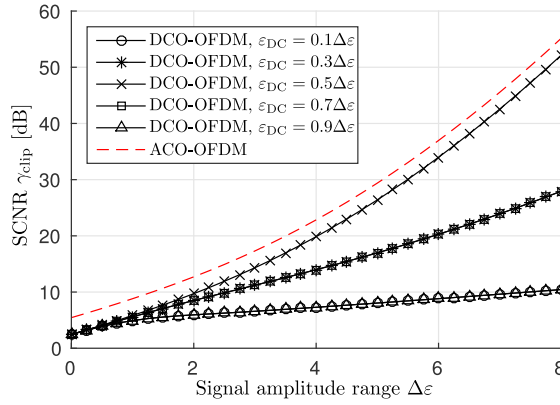
Fig. 13. Signal-to-clipping noise ratio varies with $\Delta\varepsilon$.

$$
\begin{aligned}
\sigma_{\text{clip}}^2 &= \varepsilon_{\min}^2(1 - \mathcal{Q}(\varepsilon_{\min})) + \varepsilon_{\max}^2\mathcal{Q}(\varepsilon_{\max}) + \varepsilon_{\min}f_{\mathcal{N}}(\varepsilon_{\min}) - \varepsilon_{\max}f_{\mathcal{N}}(\varepsilon_{\max}) - \eta_{\text{clip}}^2 \\
&+ \mathcal{Q}(\varepsilon_{\min}) - \mathcal{Q}(\varepsilon_{\max}) - (\varepsilon_{\min}(1 - \mathcal{Q}(\varepsilon_{\min})) + \varepsilon_{\max}\mathcal{Q}(\varepsilon_{\max}) + f_{\mathcal{N}}(\varepsilon_{\min}) - f_{\mathcal{N}}(\varepsilon_{\max}))^2.
\end{aligned}
\tag{32}
$$

A parameter denoted as $\Delta\varepsilon$ is defined to evaluate the effective signal amplitude range. In the case of DCO-OFDM, $\Delta\varepsilon = \varepsilon_{\max} - \varepsilon_{\min}$. In the case of ACO-OFDM, despite the clipping of negative samples, the missing samples can be recovered at the receiver side. Therefore, the effective signal range should be $\Delta\varepsilon = 2\varepsilon_{\max}$. Consider $\Delta\varepsilon$ as given parameters, the required normalised optical output power $\frac{\overline{P}_{\text{opt}}}{\eta_{\text{led}}\sigma_x}$ is calculated and the results are shown in Fig. 14. The figure shows that with the increase of $\Delta\varepsilon$, the required output optical power increases. For the same signal amplitude range, DCO-OFDM requires a much higher optical output power relative to the case of ACO-OFDM. Furthermore, with the increase of the DC-bias level ε_{DC}, the required output optical power increases in the DCO-OFDM system.

In the calculation of η_{clip} and σ_{clip}^2 in ACO-OFDM, the recovered signal at the receiver side is considered. Therefore, $\varepsilon_{\min} = -\varepsilon_{\max}$ is used in the calculation. In order to evaluate the clipping distortion with different clipping configurations, the signal-to-clipping noise ratio (SCNR) is defined as: $\gamma_{\text{clip}} = \frac{\xi^2\eta_{\text{clip}}^2}{\sigma_{\text{clip}}^2}$. Fig. 13 shows how the SCNR varies with $\Delta\varepsilon$. This shows that in order to avoid significant clipping distortion, $\Delta\varepsilon$ has to be sufficiently large. It also shows that to achieve the same SCNR, ACO-OFDM requires less $\Delta\varepsilon$ than DCO-OFDM. In the cases of DCO-OFDM, with the same $\Delta\varepsilon$, a DC-bias of $\varepsilon_{\text{DC}} = 0.5\Delta\varepsilon$ offers the lowest clipping distortion.

On the one hand, the results shown in Fig. 14 imply that with a limited average optical output $\overline{P}_{\text{opt}}$, the effective output signal strength gets weaker with the increase of $\Delta\varepsilon$. On the other hand, the results shown in Fig. 13 imply that less clipping distortion can be achieved with a higher value of $\Delta\varepsilon$. Therefore, there is a trade-off between signal strength and clipping distortion.

3.6. Optical power requirement

One of the important design criterium is how much optical output power is required. According to (27) and (23), the output optical power can be calculated as:
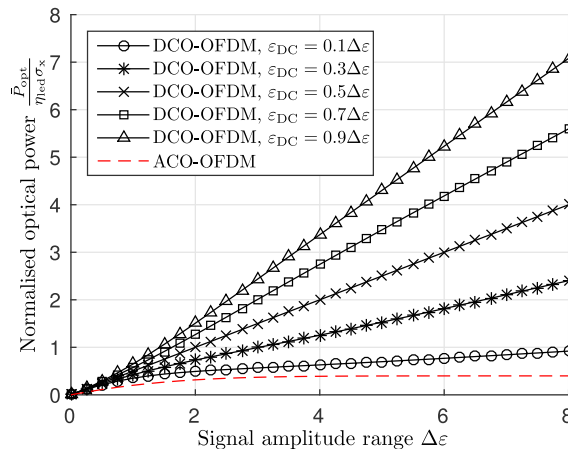

Fig. 14. Normalised optical output power varies with $\Delta\varepsilon$.

$$\overline{P}_{\text{opt}} = \eta_{\text{led}}\mathbb{E}_t[\sigma_{\text{x}}(\mathscr{V}(x(t)) + \varepsilon_{\text{DC}})] = \eta_{\text{led}}\sigma_{\text{x}}(\mathbb{E}_t[\mathscr{V}(x(t))] + \varepsilon_{\text{DC}}), \tag{33}$$

where $\mathbb{E}_t[\mathscr{V}(x(t))]$ can be calculated based on the characteristics of truncated Gaussian distribution as [111]:

$$\mathbb{E}[\mathscr{V}(x(t))] = \varepsilon_{\max}\mathbb{P}[x > \varepsilon_{\max}] + \varepsilon_{\min}\mathbb{P}[x < \varepsilon_{\min}] + \int_{\varepsilon_{\min}}^{\varepsilon_{\max}} x f_{\mathscr{N}}(x)\mathrm{d}x = \varepsilon_{\min}(1 - \mathscr{Q}(\varepsilon_{\min})) + \varepsilon_{\max}\mathscr{Q}(\varepsilon_{\max}) + f_{\mathscr{N}}(\varepsilon_{\min}) - f_{\mathscr{N}}(\varepsilon_{\max}) \tag{34}$$

Note that in the calculation of $\mathbb{E}[\mathscr{V}(x(t))]$ with ACO-OFDM, $\varepsilon_{\min} = \varepsilon_{\text{DC}} = 0$.

3.6.1. Colour modulation and wavelength division multiplexing

The use of RGB sources to provide white and variable colour illumination offers the possibility of either sending independent data streams on each colour, effectively coarse wavelength division multiplexing (WDM), or using the colour degree of freedom to encode information, known as colour shift keying. A number of WDM experiments have been reported, with some of the highest aggregate VLC data rates [69–71,108]. In these cases, bulk optics was used to combine the separate signals to provide white light, and similar optical systems to separate the channels at the receiver. Similar experiments have also been reported using laser sources. In Ref. [118] an integrated receiver that uses pn junctions at different depths in a silicon substrate is reported. The filtering effect of the semiconductor offers sufficient discrimination to separate several channels. Such innovation is required to create compact approaches to allow the widespread adoption of WDM. Colour shift keying sends information as pulses of a particular colour, as defined by the weighted combination of the LEDs that create it. Several different methods have been reported [119], including an implementation in the IEEE 802.15.7 standard [120].

3.6.2. Optical multiple-input multiple output (MIMO)

In a typical lighting installation, there are multiple LEDs chips within each luminaire and multiple luminaires in each installation. This potentially allows multiple information streams to be sent from each LED chip within one luminaire, and also different luminaires to send different information. Multiple detectors are required to decode the information at the receiver, as well as relatively complex signal processing. Fig. 15 shows the principles of optical MIMO. Light from a number of sources falls on a number of detectors, and the channel gains of each of the possible paths are measured using a training sequence. In operation independent data is sent on each
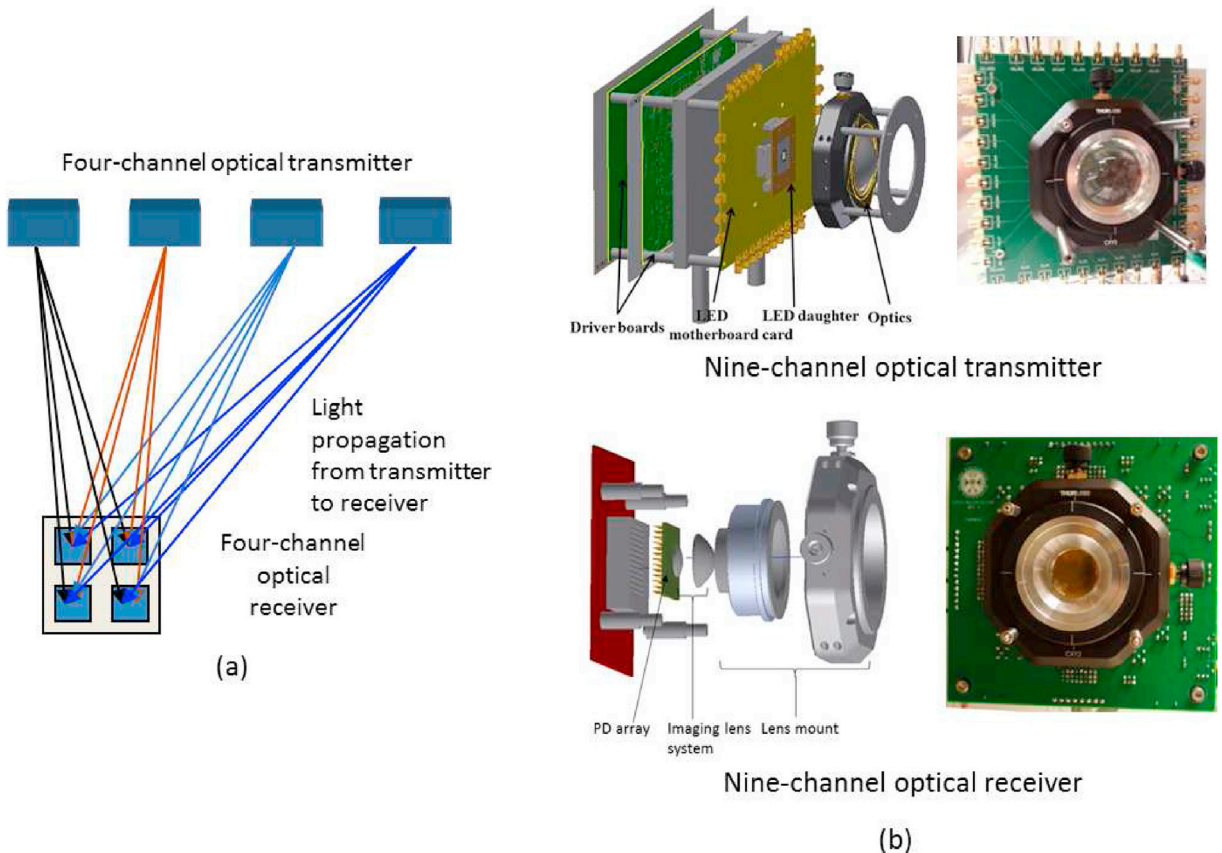

Fig. 15. (a) Figure showing principle of optical MIMO. (b) Integrated MIMO components.

channel, and the receivers detect a combination of each of these signals. The resulting channel matrix, together with the received data can be used to recover the original signal [101,102]. The alternative approach is to encode information in the spatial position of the source, known as spatial modulation [121]. At its simplest this is sending data on only one source at one time, and using a receiver structure that decodes both the data, and the position from which it was sent. The position adds extra degrees of freedom and hence data rate. More generalized schemes have been developed and analysed [122,123]. Both MIMO and spatial modulation rely on the ability of the receiver to determine where the light came from, as measured by how different signals from different sources are at the receiver. Angle diversity and imaging receiver structures [124,125] are often used in such systems for this reason.

What has been described and discussed in this section are fundamental LiFi technology building blocks which enable high speed data transmission between a static transmitter and a static receiver, i.e., fixed point-to-point wireless transmission systems with single or multiple transmitter and receiver elements. The vision of fully networked LAC networks as introduced in section 2 means the transition of a single static point-to-point VLC communication link to mobile point-to-multipoint and multipoint-to-point multiuser, networked wireless communications based on VLC. This has created a new area of research as these additional problems have to be solved.

A consequence of the existence of multiple LiFi APs (i.e., LiFi enabled luminaires) and a plurality of roaming users that will remain connected is the detrimental effect of CCI. CCI diminishes the SINR as shown in Fig. 18 and, hence, the available data rate. As discussed, CCI occurs when two neighbouring LiFi APs transmit independent signals using the same light spectrum to different users. Techniques to limit CCI in LAC networks are, therefore, of paramount importance to enable LiFi connected mobile users. To avoid that a LiFi network deployment offsets the massive advancements in gigabit point-to-point wireless data transmission by light. This important aspect is discussed in the following section.

4. Cell deployments and spatial reuse

In Section 3.3.3, it is noted that the actual channel depends on the position and the orientation of transmitters and receivers. Therefore, the channel frequency response $H_i(k)$ and the performance of the LAC network strongly dependents on the spatial deployment of the APs [126,127]. CCI is one of the most important factors with respect to downlink performance, and the significance of CCI is determined directly by the distance from the interfering source to the desired receiver. A *reuse distance* is defined to quantify this physical separation, and this depends on the actual AP deployment scenario. Various models have been reported in literature, and these are reviewed below.

4.1. Different cell deployments

In RF cellular system analyses, a number of models have been considered. The Wyner model is a one-dimensional (1-D) model, which defines the AP on a linear array [128]. It offers good tractability for mathematical analyses. However, the over-simplification causes a considerable accuracy issue. The Wyner model is suitable for studying the network that extends in one dimension, such as cellular systems along a highway or a railway. The most commonly used model is a grid-based model [32]. In a grid-based model, APs are placed on a 2-dimensional (D) hexagonal or square grid. Grid-based models offer full coverage 2-D layouts, and they are widely used in system level Monte-Carlo simulations. However, these models do not fully reflect real-world deployment scenarios. In practice, the placement of APs is subject to a number of extra constraints, such as geometric limitation, population density and output power. Therefore, non-homogeneous topologies of APs has been proposed [129,130], and tools available in stochastic geometry can be used in the analysis to get tractable result. The homogeneous Poisson Point Process (PPP) has been proposed in Ref. [131] to model the cell deployment as a pessimistic practical approximation. However, the case that two APs are placed next to each other may only happen in rare occasions. To compensate the drawback of homogeneous PPP cell deployment, point processes, such as the hard-core point process (HCPP), offer better real-world approximation, and, therefore, these tools have recently been considered in cellular system analyses [132].

Here we consider two grid-based models and two point process-based models. The grid-based model includes the hexagonal (HEX) and square cell deployments as shown in Fig. 16 (a) and (c). Square cell deployment is the simplest layout, which is perfectly compatible to a cuboid room. It has been used in many LiFi networking studies and practical lighting networks. HEX cell deployment is less common in lighting networks, but it is a desired layout for LAC networks as a hexagonal shape offers a good approximation to a circle which corresponds to the profile of a light cone when lights are placed in the ceiling and pointing downwards. An optimised performance is expected with a HEX cell deployment, but it may require extra engineering work to redesign the lighting infrastructure in a room. The considered point process based models include the homogeneous PPP cell deployment and the Matérn type I HCPP cell deployment as shown in Fig. 16 (b) and (d). The irregular placement of luminaries is mainly motivated by the following considerations: firstly, the placement of a luminaire may be limited by the wiring structure in the room. Secondly, in some cases, non-uniform illumination is required, which means that the lighting is enhanced in certain parts of the room. Also, even for a uniform cell deployment, a user may be absent in some cells. In that case, the downlink transmission can be switched off, which effectively results in a non-uniform cell deployment. The case with PPP cell deployment is expected to offer the worst case performance, and in the case with HCPP cell deployment, the consideration that two lamps are not co-located is included. In LAC network cell deployment modelling, it should be noted that a practical LAC network is bounded by the room edges.

4.2. Spatial reuse plan

Another important factor is the spatial reuse plan of the transmission resources. In order to mitigate CCI in a cellular network, a common method is to divide the entire network into multiple cell clusters [32]. Fig. 17 shows a HEX cellular network as an example. A
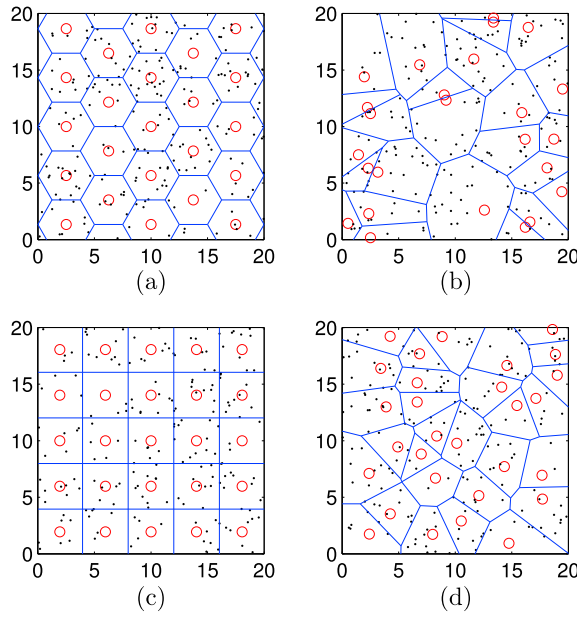
Fig. 16. Different cell deployments considered in LAC networks. (a) HEX cell deployment. (b) Homogeneous PPP cell deployment. (c) Square cell deployment. (d) HCPP cell deployment.

cluster consists of κ_{rf} cells [31]. The different colours of the cells in the cluster show that the UEs in each cell use orthogonal transmission resources (in time, frequency, wavelength, and/or space). The network is formed by tessellation with the cell cluster. This method leads to a decrease in the number of neighbouring cells using the same transmission resources as shown in Fig. 17. It results in a lower CCI level, but also causes a decrease in the spectral efficiency (available transmission resource per cell). This method is also known as static resource partitioning. The number of cells in a cell cluster κ_{rf} is defined as the spatial reuse factor, which is a key parameter to the performance of a cellular network. Note that the case of $\kappa_{rf} = 1$ is also known as universal frequency reuse (UFR). Typically, $\kappa_{rf} \leq 3$ results in good compromise in dense networks.

4.3. Downlink SINR in LiFi attocell networks

In order to evaluate the downlink performance of a LAC network, it is essential to determine the downlink SINR. A number of other important downlink system metrics, such as cell data rate, SINR statistics, require the SINR calculation for a specified link setup as a baseline. In a LAC downlink system, the SINR on subcarrier k can be defined as:

$$\gamma(k) = \frac{P_{\text{elec},0}(k)}{\sum_{i \in I} P_{\text{elec},i}(k) + P_{\text{elec},0}^{\text{clip}}(k) + \sigma_{\text{Rx}}^2}, \tag{35}$$

where $P_{\text{elec},0}(k)$ denotes the received desired signal power; $P_{\text{elec},i}(k)$ denotes the received interfering signal power from the ith AP;
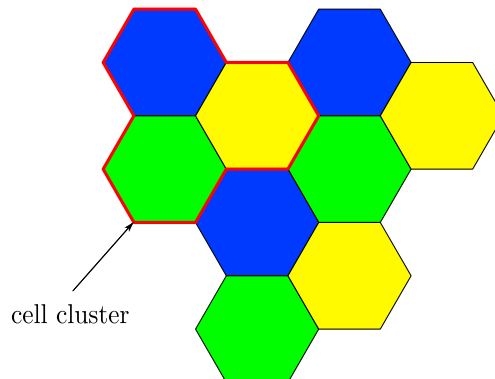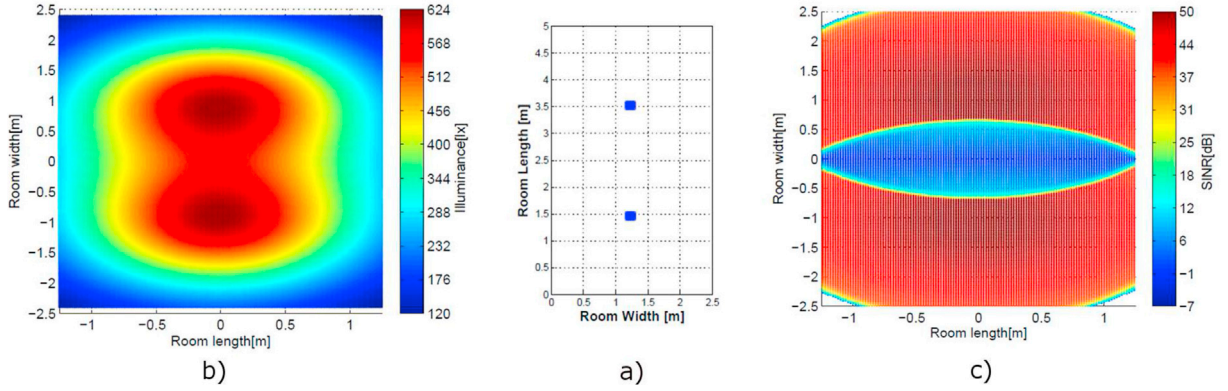

Fig. 17. An example of spatial reuse plan.

Fig. 18. A room of size 2.5 m × 5 m is equipped with two LiFi luminaires installed at 3 m height pointing vertically downwards. The LiFi luminaires are illustrated by two blue squares in subplot a). Both luminaires use the same visible light spectrum to transmit independent information. Vertically upwards pointing receivers at 0.75 m desk height are assumed. The illuminance at desk height is illustrated in subplot b). The resulting SINR assuming a receiver FoV of 45° is depicted in subplot c). (For interpretation of the references to colour in this figure legend, the reader is referred to the web version of this article.)

$P_{\text{elec},0}^{\text{clip}}(k)$ denotes the power of the received clipping noise. The received signal, $P_{\text{elec},0}(k)$ can be calculated as follows:

$$P_{\text{elec},0}(k) = \mathbb{E}\left[\left|\eta_{\text{pd}}\eta_{\text{led}}\sigma_x\eta_{\text{clip}}X_0(k)H_0(k)\right|^2\right] = \eta_{\text{pd}}^2\eta_{\text{led}}^2\sigma_x^2\eta_{\text{clip}}^2\xi^2|H_0(k)|^2. \tag{36}$$

Note that $\mathbb{E}[|X_0(k)|^2] = \xi^2$. Similarly, the received interfering signal power on subcarrier k from AP i can be determined as follows:

$$P_{\text{elec},i}(k) = \mathbb{E}\left[\left|\eta_{\text{pd}}\eta_{\text{led}}\sigma_x\left(\eta_{\text{clip}}X_i(k) + N_{\text{clip},i}(k)\right)H_i(k)\right|^2\right] = \eta_{\text{pd}}^2\eta_{\text{led}}^2\sigma_x^2\left(\eta_{\text{clip}}^2 + \sigma_{\text{clip}}^2\right)|H_i(k)|^2. \tag{37}$$

In the calculation of (37), it is worth noting that $\mathbb{E}[|X_i(k)|^2] = 1$. This is because $X_i(k)$ is assumed to be converted to a complex Gaussian signal. The power of the received clipping noise components $P_{\text{elec},0}^{\text{clip}}(k)$ can be calculated as follows:

$$P_{\text{elec},0}^{\text{clip}}(k) = \mathbb{E}\left[\left|\eta_{\text{pd}}\eta_{\text{led}}\sigma_x N_{\text{clip},i}(k)H_0(k)\right|^2\right] = \eta_{\text{pd}}^2\eta_{\text{led}}^2\sigma_x^2\sigma_{\text{clip}}^2|H_0(k)|^2. \tag{38}$$

By inserting (36), (37) and (38) into (35), the SINR expression can be expanded to yield:

$$\gamma(k) = \frac{\eta_{\text{pd}}^2\eta_{\text{led}}^2\sigma_x^2\eta_{\text{clip}}^2|H_0(k)|^2\xi^2}{\sigma_{\text{Rx}}^2 + \eta_{\text{pd}}^2\eta_{\text{led}}^2\sigma_x^2|H_0(k)|^2\sigma_{\text{clip}}^2 + \eta_{\text{pd}}^2\eta_{\text{led}}^2\sigma_x^2\left(\eta_{\text{clip}}^2 + \sigma_{\text{clip}}^2\right)\sum_{i\in I}|H_i(k)|^2}$$
$$= \left(\left(\frac{\eta_{\text{clip}}^2\xi^2|H_0(k)|^2}{\left(\eta_{\text{clip}}^2 + \sigma_{\text{clip}}^2\right)\sum_{i\in I}|H_i(k)|^2 + \frac{\sigma_{\text{Rx}}^2}{\eta_{\text{pd}}^2\eta_{\text{led}}^2\sigma_x^2}}\right)^{-1} + \frac{\sigma_{\text{clip}}^2}{\eta_{\text{clip}}^2\xi^2}\right) \tag{39}$$

where the term $\frac{\sigma_{\text{clip}}^2}{\eta_{\text{clip}}^2\xi^2}$ is the reciprocal of SCNR. According to (9), the channel gain on subcarrier k can be written as:

$$|H(k)|^2 = |H_{\text{fe}}(k)|^2|H_{\text{fs}}(k)|^2. \tag{40}$$

According to the approximation function (10), $|H_{\text{fe}}(k)|^2$ can be found:

$$|H_{\text{fe}}(k)|^2 = \exp\left(-\frac{kF_s}{KF_{\text{fe}}}\right), \tag{41}$$

for $k = 1, 2, \cdots, \tilde{K}$. In addition, the noise variance can be written as $\sigma_{\text{Rx}}^2 = \frac{N_0 F_s}{\xi^2}$. Therefore, the SINR can be rewritten as follows:

$$\gamma(k) = \left(\left(\frac{\eta_{\text{clip}}^2\xi^2|H_{\text{fs},0}(k)|^2}{\left(\eta_{\text{clip}}^2 + \sigma_{\text{clip}}^2\right)\sum_{i\in I}|H_{\text{fs},i}(k)|^2 + \frac{N_0 F_s\exp\left(\frac{kF_s}{KF_{\text{fe}}}\right)}{\xi^2\eta_{\text{pd}}^2\eta_{\text{led}}^2\sigma_x^2}}\right)^{-1} + \frac{\sigma_{\text{clip}}^2}{\eta_{\text{clip}}^2\xi^2}\right)^{-1}, \tag{42}$$

The configuration of $\eta_{\text{led}}^2\sigma_x^2$ is related to the characteristics of the LED. If the limiting factor is the available average optical output power, the value of $\eta_{\text{led}}^2\sigma_x^2$ can be calculated based on (33):

$$\eta_{\text{led}}^2 \sigma_x^2 = \frac{\overline{P}_{\text{opt}}^2}{\left(\mathbb{E}_t[\mathcal{V}(x(t))] + \varepsilon_{\text{DC}}\right)^2}. \tag{43}$$

If the limiting factor is the linear dynamic range with a maximum optical output power of $P_{\text{opt,max}}$, the value of $\eta_{\text{led}}^2 \sigma_x^2$ can be calculated based on (26) and (28):

$$\eta_{\text{led}}^2 \sigma_x^2 = \frac{P_{\text{opt,max}}^2}{\left(\varepsilon_{\text{DC}} + \varepsilon_{\text{max}}\right)^2}. \tag{44}$$

Fig. 18 visualises CCI in a simple two-cell scenario. Two LiFi luminaires transmit simultaneously using the same visible light spectrum – see Fig. 18 a). This means there is only a single interferer, and this is different from multi-cell topologies shown in Fig. 16. The purpose of this simple example is to illustrate the basic impact of CCI in a LiFi network.

A unique feature of LiFi is that it combines illumination and data communication by using the same device. Fig. 18 b) shows the resulting illuminance at desk level of 0.75 m. In the particular example, the lights are placed such that within the plane at desk height, 90% of the area achieves an illuminance of 400 lux based on a given illumination requirement. Fig. 18 c) depicts the resulting SINR. The region where the light cones overlap is subject to strong CCI, and the SINR drops significantly. It is interesting to note that the SINR can vary by about 30 dB within a few centimeters. This example also highlights that the peak SINR can be in region of 50 dB which is two to three orders of magnitude higher than the peak SINR in RF based wireless systems. The achievable data rate strongly depends on the location of the receiver and also on the FoV of the receiver [133]. Interference mitigation techniques are required to ensure within the region of strong CCI, a mobile station can also achieve high SINR, and this is a non-trivial problem which involves signal processing such as successive interference cancellation [134]. Moving on, Fig. 19 shows the cumulative density function (CDF) of achieved SINR by different system setups considering HEX and PPP cell deployments with DCO-OFDM. The cell radius in these multi-cell deployment scenarios is denoted by R. The SINR at DC is shown as an example, and the SINR at other frequencies decreases with an increase of frequency due to the low-pass effect of the front-end elements. The values shown in Table 1 are used if the system parameter is not specified for each setup, where the configuration of F_s and F_{fe} are in accordance with the setup in Ref. [93].

The first important observation is that the actual cell deployment scenario has a significant impact on the achievable SINR, and thus on the maximum achievable data rate. This means, that if the LAC system is not designed carefully, all the significant improvements in data rates in link level systems over the last 10 years can easily be offset when moving from point-to-point VLC to networked LiFi. In setup 1, $R = 2.5$ m, $\phi_{1/2} = 40°$ and $\kappa_{\text{rf}} = 1$. The results for both the HEX and the PPP networks are shown. It can be observed as expected that with the same system configuration, a random PPP network performs worse than a regular HEX network. In addition, the considered background light level is 100 lux in illuminance. Therefore, the APs operate with their full power to provide enough illumination. The highest SINR of above 30 dB shows that the noise at the receiver side causes little effect to the system performance. In setup 2, the signal amplitude range is modified to 5. This results in a more serious signal clipping distortion. Consequently, the highest SINR in this system is limited by the clipping noise. In setup 3, $R = 3$ m, $\phi_{1/2} = 50°$, $\kappa_{\text{rf}} = 3$. All other parameters are the same as in setup 1. The high reuse factor leads to a lower level of CCI and the overall SINR level improved significantly compared with that of setup 1. Therefore, the corresponding SINR is improved compared to the case of setup 1 for both HEX and PPP networks. Setup 4 considers a special case with sufficient illumination from ambient light with an illuminance of 1000 lux. Thus, the AP works in a dimmed mode with only 15% of its normal output. Due to the reduced signal power and increased noise level, the overall SNR level is decreased to a range of -3 dB to 22 dB. This demonstrates that the system will work under strong background light conditions, and also when the lights are dimmed.
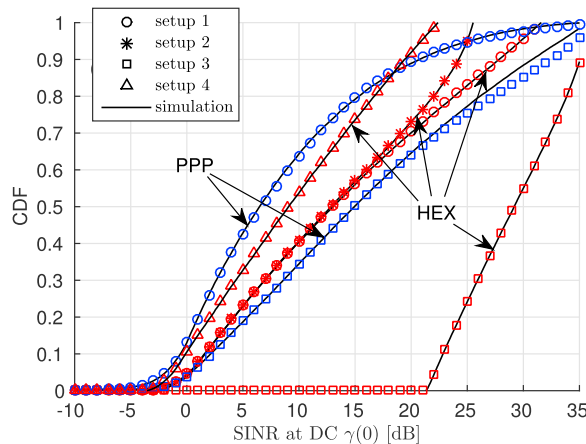

Fig. 19. The CDF of the SINR at DC. Setup 1: $R = 2.5$ m, $\phi_{1/2} = 40°$, $\kappa_{\text{rf}} = 1$, 100% output. Setup 2: same as setup 1 except $\Delta\varepsilon = 5$. Setup 3: $R = 3$ m, $\phi_{1/2} = 50°$, $\kappa_{\text{rf}} = 3$, 100% output. Setup 4: same as setup 1 except 15% output and 1000 lux ambient light illuminance. Other parameters are listed in Table 1 if they are not specified.

Table 1
Default LAC downlink system parameters.

Parameters	Symbol	Values
Transmitter height	z_s	3 [m]
Receiver height	z_r	0.75 [m]
Receiver FoV	ψ_max	90°
Modulation bandwidth	F_s	360 [MHz]
Front-end device bandwidth factor	F_fe	31.7 [MHz]
DC-bias level	e_DC	0.5
Signal amplitude range	$\Delta\varepsilon$	6.4
PD responsivity	η_pd	0.4 [A/W]
PD physical area	A_pd	1 [cm^2]
Number of subcarriers	K	512
Cell centre illuminance from AP	$\bar{E}_\text{v}$	500 [lux]
Background illuminance	$E_\text{v,bg}$	100 [lux]
Absolute temperature	T	300 [K]
Receiver load resistance	R_L	500 [Ω]

5. Conclusion

With the popularity of smart devices, there is a growing demand for wireless communications resulting from new applications such as virtual reality and high definition TV. In addition, it is predicted that the IoT and Industry 4.0 will create an explosion in the number and diversity of devices. All these new trends will require new means of providing wireless communications in a wide range of environments. A crucial aspect of this is the allocation of a new spectrum for additional capacity. LiFi networks, using visible light communications, have the potential to provide this with high capacity in the environments with very high user and device density. This paper highlights the challenges of providing wireless communications networks using light, including interference and deployment strategies, and introduces a framework for determining the key parameters in their performance. Specifically, it has shown that an integrated and holistic approach is needed to address these challenges. Optical devices, and their arrangement in an optical transceiver, affect the performance of networking techniques such as interference mitigation algorithms and multiuser access techniques. Similarly, optimum networking performance imposes specific requirements on optical devices and optical sub-systems. Therefore, the techniques that have led to record data rates in fixed point-to-point link-level VLC systems may only be sub-optimum in LiFi network deployments. Therefore, further work in this area from researchers in devices and networks is required.

Acknowledgement

References

[1] T.S. Rappaport, S. Sun, R. Mayzus, H. Zhao, Y. Azar, K. Wang, G.N. Wong, J.K. Schulz, M. Samimi, F. Gutierrez, Millimeter wave mobile communications for 5g cellular: it will work!, IEEE Access 1 (2013) 335–349.

[2] J. Jiang, Y. Huo, F. Jin, P. Zhang, Z. Wang, Z. Xu, H. Haas, L. Hanzo, Video streaming in the multiuser indoor visible light downlink, IEEE Access 3 (2015) 2959–2986, http://dx.doi.org/10.1109/ACCESS.2015.2513010.

[3] S. Karp, E.L. O'Neill, R.M. Gagliardi, Communication theory for the free-space optical channel, Proc. IEEE 58 (10) (1970) 1611–1626, http://dx.doi.org/10.1109/PROC.1970.7985.

[4] W. S. Rabinovich, C. I. Moore, H. R. Burris, J. L. Murphy, M. R. Suite, R. Mahon, M. S. Ferraro, P. G. Goetz, L. M. Thomas, C. Font, G. C. Gilbreath, B. Xu, S. Binari, K. Hacker, S. Reese, W. T. Freeman, S. Frawley, Free Space Optical Communications Research at the U. S. Naval Research Laboratory, Free-Space Laser Communication Technologies Xxii 7587. http://dx.doi.org/10.1117/12.843682.

[5] F. Heine, H. Kämpfner, R. Lange, R. Czichy, M. Lutzer, R. Meyer, Laser communication applied for EDRS, the european data relay system, CEAS Space J. 2 (1) (2011) 85–90.

[6] I. K. Son, S. Mao, A Survey of Free Space Optical Networks, Digital Communications and Networks. http://dx.doi.org/10.1016/j.dcan.2016.11.002.

[7] F.R. Gfeller, U. Bapst, Wireless in-house data communication via diffuse infrared radiation, Proc. IEEE 67 (11) (1979) 1474–1486.

[8] P. Barker, A.C. Boucouvalas, Performance modeling of the IrDA protocol for infrared wireless communications, IEEE Commun. Mag. 36 (12) (1998) 113–117, http://dx.doi.org/10.1109/35.735888.

[9] M. Faulwasser, F. Deicke, T. Schneider, 10 gbit/s Bidirectional Optical Wireless Communication Module for Docking Devices, Globecom Workshops (Gc Wkshps), 2014, pp. 512–517.

[10] G.W. Marsh, J.M. Kahn, Performance evaluation of experimental 50-Mb/s diffuse infrared wireless link using on-off keying with decision-feedback equalization, IEEE Trans. Commun. 44 (11) (1996) 1496–1504.

[11] J.B. Carruthers, J.M. Kahn, Angle diversity for nondirected wireless infrared communication, IEEE Trans. Commun. 48 (6) (2000) 960–969.

[12] S. Jivkova, M. Kavehrad, Holographic optical receiver front end for wireless infrared indoor communications, Appl. Opt. 40 (17) (2001) 2828–2835.

[13] D. O'Brien, R. Turnbull, H. Le Minh, G. Faulkner, O. Bouchet, P. Porcon, M. El Tabach, E. Gueutier, M. Wolf, L. Grobe, J. Li, High-speed optical wireless demonstrators: conclusions and future directions, J. Light. Technol. 30 (13) (2012) 2181–2187.

[14] D.K. Borah, A.C. Boucouvalas, C.C. Davis, S. Hranilovic, K. Yiannopoulos, A review of communication-oriented optical wireless systems, Eurasip J. Wirel. Commun. Netw. 2012 (1) (2012) 91.

[15] C.W. Oh, Z.Z. Cao, E. Tangdiongga, T. Koonen, Free-space Transmission with Passive 2D Beam Steering for Multi-gigabit-per-second per-beam Indoor Optical Wireless Networks, Opt. Express 24 (17) (2016) 19211–19227.

[16] K. Wang, A. Nirmalathas, C. Lim, K. Alameh, E. Skafidas, Full-duplex gigabit indoor optical wireless communication system with CAP modulation, IEEE Photonics Technol. Lett. 28 (7) (2016) 790–793.

[17] A. Gomez, K. Shi, C. Quintana, R. Maher, G. Faulkner, P. Bayvel, B.C. Thomsen, D.O. Brien, Design and demonstration of a 400 gb/s indoor optical wireless communications link, J. Light. Technol. 34 (22) (2016) 5332–5339.

[18] European Commission, Technical Briefing: Phasing Out Incandescent Bulbs in the EU, Sep. 2008. Retrieved from, http://ec.europa.eu.

[19] P.H. Pathak, X. Feng, P. Hu, P. Mohapatra, Visible light communication, networking, and sensing: a survey, potential and challenges, IEEE Commun. Surv. Tutorials 17 (4) (2015) 2047–2077, http://dx.doi.org/10.1109/COMST.2015.2476474.

[20] T. Komine, M. Nakagawa, Fundamental analysis for visible-light communication system using led lights, IEEE Trans. Consumer Electron. 50 (1) (2004) 100–107, http://dx.doi.org/10.1109/TCE.2004.1277847.

[21] H. Haas, Wireless Data from Every Light Bulb, TED Website, Aug. 2011. URL, http://bit.ly/tedvlc.

[22] D. Tsonev, H. Chun, S. Rajbhandari, J.J.D. McKendry, S. Videv, E. Gu, M. Haji, S. Watson, A.E. Kelly, G. Faulkner, M.D. Dawson, H. Haas, D. O'Brien, A 3-Gb/s single-LED OFDM-based wireless VLC link using a Gallium Nitride μLED, IEEE photon, Technol. Lett. 26 (7) (2014) 637–640, http://dx.doi.org/10.1109/LPT.2013.2297621.

[23] G. Cossu, A.M. Khalid, P. Choudhury, R. Corsini, E. Ciaramella, 3.4 Gbit/s visible optical wireless transmission based on RGB LED, Opt. Express 20 (2012) B501–B506.

[24] IEEE Std 802.15.7–2011, IEEE Standard for Local and Metropolitan Area Networks, Part 15.7: Short-range Wireless Optical Communication Using Visible Light, 2011.

[25] D. Karunatilaka, F. Zafar, V. Kalavally, R. Parthiban, Led based indoor visible light communications: state of the art, IEEE Commun. Surv. Tutorials 17 (3) (2015) 1649–1678, http://dx.doi.org/10.1109/COMST.2015.2417576.

[26] S. Wu, H. Wang, C.H. Youn, Visible light communications for 5G wireless networking systems: from fixed to mobile communications, IEEE Netw. 28 (6) (2014) 41–45, http://dx.doi.org/10.1109/MNET.2014.6963803.

[27] A. Sevincer, A. Bhattarai, M. Bilgi, M. Yuksel, N. Pala, Lightnets: smart lighting and mobile optical wireless networks – a survey, IEEE Commun. Surv. Tutorials 15 (4) (2013) 1620–1641, http://dx.doi.org/10.1109/SURV.2013.032713.00150.

[28] H. Haas, L. Yin, Y. Wang, C. Chen, What is LiFi? J. Lightw. Technol. 34 (6) (2016) 1533–1544, http://dx.doi.org/10.1109/JLT.2015.2510021.

[29] W. Ni, R.P. Liu, I.B. Collings, X. Wang, Indoor cooperative small cells over ethernet, IEEE Commun. Mag. 51 (9) (2013) 100–107, http://dx.doi.org/10.1109/MCOM.2013.6588657.

[30] A. Papaioannou, F.N. Pavlidou, Evaluation of power line communication equipment in home networks, IEEE Syst. J. 3 (3) (2009) 288–294, http://dx.doi.org/10.1109/JSYST.2009.2023202.

[31] V.H. McDonald, The cellular concept, Bell Syst. Tech. J. (1979) 15–49.

[32] A. Goldsmith, Wireless Communications, Cambridge University Press, 2005.

[33] D. Simeonidou, R. Nejabati, M.P. Channegowda, Software defined optical networks technology and infrastructure: enabling software-defined optical network operations, in: Optical Fiber Communication Conference and Exposition and the National Fiber Optic Engineers Conference (OFC/NFOEC), vol. 2013, 2013, pp. 1–3, http://dx.doi.org/10.1364/OFC.2013.OTh1H.3.

[34] M. Ayyash, H. Elgala, A. Khreishah, V. Jungnickel, T. Little, S. Shao, M. Rahaim, D. Schulz, J. Hilt, R. Freund, Coexistence of WiFi and LiFi toward 5G: concepts, opportunities, and challenges, IEEE Commun. Mag. 54 (2) (2016) 64–71, http://dx.doi.org/10.1109/MCOM.2016.7402263.

[35] M.B. Rahaim, A.M. Vegni, T.D.C. Little, A Hybrid Radio Frequency and Broadcast Visible Light Communication System, IEEE GLOBECOM Workshops, 2011, pp. 792–796.

[36] B. Ghimire, H. Haas, Self-organising interference coordination in optical wireless networks, EURASIP J. Wirel. Commun. Netw. 1(131).

[37] Z. Chen, N. Serafimovski, H. Haas, Angle diversity for an indoor cellular visible light communication system, in: Proc. of IEEE Veh. Technol. Conf., Seoul, South Korea, 2014, pp. 1–5, http://dx.doi.org/10.1109/VTCSpring.2014.7022832.

[38] C. Chen, S. Videv, D. Tsonev, H. Haas, Fractional frequency reuse in DCO-OFDM-based optical attocell networks, J. Light. Technol. 33 (19) (2015) 3986–4000, http://dx.doi.org/10.1109/JLT.2015.2458325.

[39] X. Li, R. Zhang, J. Wang, L. Hanzo, Cell-centric and user-centric multi-user scheduling in visible light communication aided networks, in: 2015 IEEE International Conference on Communications (ICC), 2015, pp. 5120–5125, http://dx.doi.org/10.1109/ICC.2015.7249136.

[40] B. Li, J. Wang, R. Zhang, H. Shen, C. Zhao, L. Hanzo, Multiuser MISO transceiver design for indoor downlink visible light communication under per-LED optical power constraints, IEEE Photonics J. 7 (4) (2015) 1–15, http://dx.doi.org/10.1109/JPHOT.2015.2446203.

[41] M. Pischella, J.C. Belfiore, Power control in distributed cooperative OFDMA cellular networks, IEEE Trans. Wirel. Commun. 7 (5) (2008) 1900–1906, http://dx.doi.org/10.1109/TWC.2008.061039.

[42] H. Marshoud, V.M. Kapinas, G.K. Karagiannidis, S. Muhaidat, Non-orthogonal multiple access for visible light communications, IEEE Photonics Technol. Lett. 28 (1) (2016) 51–54, http://dx.doi.org/10.1109/LPT.2015.2479600.

[43] L. Yin, W.O. Popoola, X. Wu, H. Haas, Performance evaluation of non-orthogonal multiple access in visible light communication, IEEE Trans. Commun. 64 (12) (2016) 5162–5175, http://dx.doi.org/10.1109/TCOMM.2016.2612195.

[44] G.W. Marsh, J.M. Kahn, Channel reuse strategies for indoor infrared wireless communications, IEEE Trans. Commun. 45 (10) (1997) 1280–1290, http://dx.doi.org/10.1109/26.634692.

[45] J. Fakidis, D. Tsonev, H. Haas, A comparison between DCO-OFDMA and synchronous one-dimensional OCDMA for optical wireless communications, in: Proc. IEEE 24th Int. Symp. Pers. Indoor and Mobile Radio Commun., London, UK, 2013, pp. 3605–3609.

[46] S. Dimitrov, H. Haas, Principles of LED Light Communications: towards Networked Li-fi, Cambridge University Press, 2015.

[47] G. Miao, J. Zander, K.W. Sung, S.B. Slimane, Fundamentals of Mobile Data Networks, Cambridge University Press, 2016.

[48] A. Ahmed, L.M. Boulahia, D. Gaiti, Enabling vertical handover decisions in heterogeneous wireless networks: a state-of-the-Art and A Classification, IEEE Commun. Surv. Tutorials 16 (2) (2014) 776–811, http://dx.doi.org/10.1109/SURV.2013.082713.00141.

[49] Y. Wang, H. Haas, Dynamic load balancing with handover in hybrid Li-Fi and Wi-Fi networks, J. Lightw. Technol. 33 (22) (2015) 4671–4682, http://dx.doi.org/10.1109/JLT.2015.2480969.

[50] O. Tipmongkolsilp, S. Zaghloul, A. Jukan, The evolution of cellular backhaul technologies: current issues and future trends, IEEE Commun. Surv. Tutorials 13 (1) (2011) 97–113, http://dx.doi.org/10.1109/SURV.2011.040610.00039.

[51] X. Ge, H. Cheng, M. Guizani, T. Han, 5G wireless backhaul networks: challenges and research advances, IEEE Netw. 28 (6) (2014) 6–11, http://dx.doi.org/10.1109/MNET.2014.6963798.

[52] L. Verma, M. Fakharzadeh, S. Choi, Backhaul need for speed: 60 GHz is the solution, IEEE Wirel. Commun. 22 (6) (2015) 114–121, http://dx.doi.org/10.1109/MWC.2015.7368832.

[53] D. Schulz, V. Jungnickel, C. Alexakis, M. Schlosser, J. Hilt, A. Paraskevopoulos, L. Grobe, P. Farkas, R. Freund, Robust optical wireless link for the backhaul and fronthaul of small radio cells, J. Light. Technol. 34 (6) (2016) 1523–1532, http://dx.doi.org/10.1109/JLT.2016.2523801.

[54] H.L. Minh, D. O'Brien, G. Faulkner, L. Zeng, K. Lee, D. Jung, Y. Oh, E.T. Won, 100-mb/s nrz visible light communications using a postequalized white led, IEEE Photonics Technol. Lett. 21 (15) (2009) 1063–1065, http://dx.doi.org/10.1109/LPT.2009.2022413.

[55] H.L. Minh, D.O. Brien, G. Faulkner, L. Zeng, K. Lee, D. Jung, Y. Oh, High-speed visible light communications using multiple-resonant equalization, IEEE Photonics Technol. Lett. 20 (14) (2008) 1243–1245.

[56] P.F. Tian, J.J.D. McKendry, E.D. Gu, Z.Z. Chen, Y.J. Sun, G.Y. Zhang, M.D. Dawson, R. Liu, Fabrication, characterization and applications of flexible vertical InGaN micro-light emitting diode arrays, Opt. Express 24 (1) (2016) 699–707.

[57] Z. Quan, D.V. Dinh, S. Presa, B. Roycroft, A. Foley, M. Akhter, D. O'Mahony, P.P. Maaskant, M. Caliebe, F. Scholz, P.J. Parbrook, B. Corbett, High bandwidth freestanding semipolar ingan/gan light-emitting diodes, IEEE Photonics J. 8 (5) (2016) 1–8, http://dx.doi.org/10.1109/JPHOT.2016.2596245.

[58] Y.F. Yin, W.Y. Lan, T.C. Lin, C. Wang, M. Feng, J.J. Huang, High-speed visible light communication using gan-based light-emitting diodes with photonic crystals, J. Light. Technol. PP 99 (2016), http://dx.doi.org/10.1109/JLT.2016.2634005, 1–1.

[59] R.X.G. Ferreira, E. Xie, J.J.D. McKendry, S. Rajbhandari, H. Chun, G. Faulkner, S. Watson, A.E. Kelly, E. Gu, R.V. Penty, I.H. White, D.C. O'Brien, M.D. Dawson, High bandwidth gan-based micro-LEDs for multi-gb/s visible light communications, IEEE Photonics Technol. Lett. 28 (19) (2016) 2023–2026, http://dx.doi.org/10.1109/LPT.2016.2581318.

[60] M.S. Islim, R.X. Ferreira, X. He, E. Xie, S. Videv, S. Viola, S. Watson, N. Bamiedakis, R.V. Penty, I.H. White, A.E. Kelly, E. Gu, H. Haas, M.D. Dawson, Towards 10 Gb/s orthogonal frequency division multiplexing-based visible light communication using a GaN violet micro-LED, Phot. Res. 5 (2) (2017) A35–A43, http://dx.doi.org/10.1364/PRJ.5.000A35.

[61] M.T. Sajjad, P.P. Manousiadis, H. Chun, D.A. Vithanage, S. Rajbhandari, A.L. Kanibolotsky, G. Faulkner, D. O'Brien, P.J. Skabara, I.D.W. Samuel, G.A. Turnbull, Novel fast color-converter for visible light communication using a blend of conjugated polymers, Am. Chem. Soc. (ACS) Photonics 2 (2) (2015) 194–199, http://dx.doi.org/10.1021/ph500451y.

[62] J.M.M. Santos, S. Rajbhandari, D. Tsonev, H. Chun, B. Guilhabert, A.B. Krysa, A.E. Kelly, H. Haas, D.C. O'Brien, N. Laurand, M.D. Dawson, Visible light communication using InGaN optical sources with AlInGaP nanomembrane down-converters, Opt. Express 24 (9) (2016) 10020–10029.

[63] I. Dursun, C. Shen, M.R. Parida, J. Pan, S.P. Sarmah, D. Priante, N. Alyami, J. Liu, M.I. Saidaminov, M.S. Alias, A.L. Abdelhady, T.K. Ng, O.F. Mohammed, B.S. Ooi, O.M. Bakr, Perovskite nanocrystals as a color converter for visible light communication, ACS Photonics 3 (7) (2016) 1150–1156, http://dx.doi.org/10.1021/acsphotonics.6b00187 arXiv, http://dx.doi.org/10.1021/acsphotonics.6b00187, http://dx.doi.org/10.1021/acsphotonics.6b00187.

[64] A. Neumann, J.J. Wierer, W. Davis, Y. Ohno, S.R.J. Brueck, J. Tsao, Four-color laser white illuminant demonstrating high color-rendering quality, Opt. Express 19 (S4) (2011) A982–A990, http://dx.doi.org/10.1364/OE.19.00A982. URL, http://www.opticsexpress.org/abstract.cfm?URI=oe-19-104-A982.

[65] D. Tsonev, S. Videv, H. Haas, Towards a 100 Gb/s visible light wireless access network, Opt. Express 23 (2) (2015) 1627–1637, http://dx.doi.org/10.1364/OE.23.001627. URL, http://www.opticsexpress.org/abstract.cfm?URI=oe-23-2-1627.

[66] L. Ulrich, Whiter brights with lasers, IEEE Spectr. 50 (11) (2013) 36–56, http://dx.doi.org/10.1109/MSPEC.2013.6655838.

[67] H. Chun, S. Rajbhandari, D. Tsonev, G. Faulkner, H. Haas, D. O'Brien, Visible light communication using laser diode based remote phosphor technique, in: IEEE International Conference on Communication Workshop, 2015, pp. 1392–1397.

[68] Y.-C. Chi, D.-H. Hsieh, C.-Y. Lin, H.-Y. Chen, C.-Y. Huang, J.-H. He, B. Ooi, S.P. DenBaars, S. Nakamura, H.-C. Kuo, G.-R. Lin, Phosphorous diffuser diverged blue laser diode for indoor lighting and communication, Sci. Rep. 5 (2015) 18690.

[69] H. Chun, S. Rajbhandari, G. Faulkner, D. Tsonev, E. Xie, J.J.D. McKendry, E. Gu, M.D. Dawson, D.C. O'Brien, H. Haas, Led based wavelength division multiplexed 10 gb/s visible light communications, J. Light. Technol. 34 (13) (2016) 3047–3052, http://dx.doi.org/10.1109/JLT.2016.2554145.

[70] Y. Wang, L. Tao, X. Huang, J. Shi, N. Chi, 8-gb/s rgby led-based wdm vlc system employing high-order cap modulation and hybrid post equalizer, IEEE Photonics J. 7 (6) (2015) 1–7, http://dx.doi.org/10.1109/JPHOT.2015.2489927.

[71] F.-M. Wu, C.-T. Lin, C.-C. Wei, C.-W. Chen, Z.-Y. Chen, H.-T. Huang, 3.22-Gb/s WDM visible light communication of a single RGB LED employing carrier-less amplitude and phase modulation, in: Optical Fiber Communication Conference and Exposition and the National Fiber Optic Engineers Conference (OFC/NFOEC), IEEE, 2013, pp. 1–3.

[72] European Standard EN 12464-1, Lighting of Indoor Work Places, Jan. 2009.

[73] BSI British Standards, BS EN 62471:2008, Sep. 2008.

[74] J.R. Meyer-Arendt, Radiometry and photometry: units and conversion factors, Appl. Opt. 7 (10) (1968) 2081–2084, http://dx.doi.org/10.1364/AO.7.002081.

[75] VESTA 165mm Recessed LED Downlighter. [link]. URL http://www.istl.com/vesta.php.

[76] 64 W LED panel (Aug. 2014). [link]. URL http://wellmaxled.com/portfolio/64-w-led-panel-light/.

[77] J. Armstrong, R.J. Green, M.D. Higgins, Comparison of three receiver designs for optical wireless communications using white leds, IEEE Commun. Lett. 16 (5) (2012) 748–751, http://dx.doi.org/10.1109/LCOMM.2012.031912.112206.

[78] W.T. Welford, R. Windston, High Collection Nonimaging Optics, Academic Press, 1989.

[79] R. Ramirez-Iniguez, R. Green, Optical antenna design for indoor optical wireless communication systems, Int. J. Commun. Syst. 18 (3) (2005) 229–245.

[80] S. Collins, D.C. O'Brien, A. Watt, High gain, wide field of view concentrator for optical communications, Opt. Lett. 39 (7) (2014) 1756–1759.

[81] P.P. Manousiadis, S. Rajbhandari, R. Mulyawan, D.A. Vithanage, H. Chun, G. Faulkner, D.C. O'Brien, G.A. Turnbull, S. Collins, I.D.W. Samuel, Wide field-of-view fluorescent antenna for visible light communications beyond the etendue limit, Optica 3 (7) (2016) 702–706.

[82] S.B. Alexander, S. Of Photo-optical Instrumentation Engineers., I. of Electrical Engineers., Optical Communication Receiver Design, Tutorial Texts in Optical Engineering, SPIE Optical Engineering Press ; Institution of Electrical Engineers, Bellingham, Wash. London, 1997.

[83] D.C. O'Brien, G. Faulkner, E.B. Zyambo, K. Jim, D.J. Edwards, P. Stavrinou, G. Parry, J. Bellon, M.J. Sibley, V.A. Lalithambika, V.M. Joyner, R.J. Samsudin, D.M. Holburn, R.J. Mears, Integrated transceivers for optical wireless communications, IEEE J. Sel. Top. Quantum Electron. 11 (1) (2005) 173–183.

[84] V.A. Lalithambika, V.M. Joyner, D.M. Holburn, R.J. Mears, Development of a CMOS 310Mb/s receiver for free space optical wireless links, Opt. Wirel. Commun. Iii 4214 (2001) 133–143.

[85] V.M. Joyner, S. Harris, S. Sonkusale, in: On the Design of Low-power Front-end Receiver Circuits for Broadband Optical Free-space Links, Ifip International Conference on Wireless and Optical Communications Networks, 2007, pp. 504–507.

[86] P. Brandl, R. Enne, T. Jukic, H. Zimmermann, Owc using a fully integrated optical receiver with large-diameter apd, IEEE Photonics Technol. Lett. 27 (5) (2015) 482–485.

[87] V.M. Joyner, J. Zeng, A CMOS imaging diversity receiver for gigabit free-space optical MIMO, Analog Integr. Circuits Signal Process. 66 (3) (2011) 371–379.

[88] D. Chitnis, L. Zhang, H. Chun, S. Rajbhandari, G. Faulkner, D. O'Brien, S. Collins, A 200 Mb/s VLC demonstration with a SPAD based receiver, in: 2015 IEEE Summer Topicals Meeting Series (SUM), 2016, pp. 226–227.

[89] Y. Li, M. Safari, R. Henderson, H. Haas, Optical OFDM with single-photon avalanche diode, IEEE Photonics Technol. Lett. 27 (9) (2015) 943–946, http://dx.doi.org/10.1109/LPT.2015.2402151.

[90] E. Sarbazi, H. Haas, Detection statistics and error performance of SPAD-based optical receivers, in: 2015 IEEE 26th Annual International Symposium on Personal, Indoor, and Mobile Radio Communications (PIMRC), 2015, pp. 830–834, http://dx.doi.org/10.1109/PIMRC.2015.7343412.

[91] H.L. Minh, D. O'Brien, G. Faulkner, L. Zeng, K. Lee, D. Jung, Y. Oh, E.T. Won, 100-Mb/s NRZ visible light communications using a postequalized white LED, IEEE Photonics Technol. Lett. 21 (15) (2009) 1063–1065, http://dx.doi.org/10.1109/LPT.2009.2022413.

[92] J. Vucic, C. Kottke, S. Nerreter, K.D. Langer, J.W. Walewski, 513 Mbit/s visible light communications link based on DMT-modulation of a white LED, J. Lightw. Technol. 28 (24) (2010) 3512–3518, http://dx.doi.org/10.1109/JSAC.2002.1007384.

[93] A.M. Khalid, G. Cossu, P. Choudhry, E. Ciaramella, 1-Gb/s transmission over a phosphorescent white LED by using rate-adaptive discrete multitone modulation, IEEE Phot. J. 4 (5) (2012) 1465–1473.

[94] M.J.N. Sibley, J. Bellon, Transit-time limitations in P-I-N photodiodes, Microw. Opt. Technol. Lett. 26 (5) (2000) 282–286.

[95] J.M. Kahn, J.R. Barry, Wireless infrared communications, Proc. IEEE 85 (2) (1997) 265–298, http://dx.doi.org/10.1109/5.554222.

[96] J. Barry, J. Kahn, W. Krause, E. Lee, D. Messerschmitt, Simulation of multipath impulse response for indoor wireless optical channels, IEEE J. Sel. Areas Commun. 11 (3) (1993) 367–379, http://dx.doi.org/10.1109/49.219552.

[97] F.J. Lopez-Hernandez, R. Perez-Jimenez, A. Santamara, Ray-tracing algorithms for fast calculation of the channel impulse response on diffuse IR wireless indoor channels, Opt. Eng. 39 (10) (2000) 2775–2780, http://dx.doi.org/10.1117/1.1287397.

[98] F.J. Lopez-Hernandez, M.J. Betancor, DUSTIN: algorithm for calculation of impulse response on IR wireless indoor channels, Electron. Lett. 33 (21) (1997) 1804–1806, http://dx.doi.org/10.1049/el:19971224.

[99] J.B. Carruthers, J.M. Kahn, Modeling of nondirected wireless infrared channels, IEEE Trans. Commun. 45 (10) (1997) 1260–1268, http://dx.doi.org/10.1109/26.634690.

[100] V. Jungnickel, V. Pohl, S. Nonnig, C. von Helmolt, A physical model of the wireless infrared communication channel, IEEE J. Sel. Areas Commun. 20 (3) (2002) 631–640, http://dx.doi.org/10.1109/49.995522.

[101] L.B. Zeng, D.C. O'Brien, H. Le Minh, G.E. Faulkner, K. Lee, D. Jung, Y. Oh, E.T. Won, High data rate multiple input multiple output (mimo) optical wireless communications using white led lighting, IEEE J. Sel. Areas Commun. 27 (9) (2009) 1654–1662.

[102] T. Fath, H. Haas, Performance comparison of mimo techniques for optical wireless communications in indoor environments, IEEE Trans. Commun. 61 (2) (2013) 733–742, http://dx.doi.org/10.1109/TCOMM.2012.120512.110578.

[103] M.D. Renzo, H. Haas, A. Ghrayeb, S. Sugiura, L. Hanzo, Spatial modulation for generalized mimo: Challenges, opportunities, and implementation, Proc. IEEE 102 (2014) 56–103, http://dx.doi.org/10.1109/JPROC.2013.2287851.

[104] S. Dimitrov, H. Haas, Information rate of OFDM-based optical wireless communication systems with nonlinear distortion, J. Lightw. Technol. 31 (6) (2013) 918–929, http://dx.doi.org/10.1109/JLT.2012.2236642.

[105] S. Dimitrov, S. Sinanovic, H. Haas, Signal shaping and modulation for optical wireless communication, J. Light. Technol. 30 (9) (2012) 1319–1328, http://dx.doi.org/10.1109/JLT.2012.2188376.

[106] M. Noshad, M. Brandt-Pearce, Hadamard-coded modulation for visible light communications, IEEE Trans. Commun. 64 (3) (2016) 1167–1175, http://dx.doi.org/10.1109/TCOMM.2016.2520471.

[107] H.C. Andrews, K.L. Caspari, A generalized technique for spectral analysis, IEEE Trans. Comput. C 19 (1) (1970) 16–25, http://dx.doi.org/10.1109/TC.1970.5008895.

[108] Y.Q. Wang, X.X. Huang, J.W. Zhang, Y.G. Wang, N. Chi, Enhanced performance of visible light communication employing 512-QAM N-SC-FDE and DD-LMS, Opt. Express 22 (13) (2014) 15328–15334.

[109] N. Bamiedakis, X. Li, J. J. D. McKendry, E. Xie, R. Ferreira, E. Gu, M. D. Dawson, R. V. Penty, I. H. White, Micro-led-based guided-wave optical links for visible light communications, In: 17th International Conference on Transparent Optical Networks (ICTON).

[110] J. Armstrong, OFDM for optical communications, J. Lightw. Technol. 27 (3) (2009) 189–204, http://dx.doi.org/10.1109/JLT.2008.2010061.

[111] S. Dimitrov, S. Sinanovic, H. Haas, Clipping noise in OFDM-based optical wireless communication systems, IEEE Trans. Commun. 60 (4) (2012) 1072–1081, http://dx.doi.org/10.1109/TCOMM.2012.022712.100493.

[112] M.Z. Afgani, H. Haas, H. Elgala, D. Knipp, Visible light communication using ofdm, 2006, in: 2nd International Conference on Testbeds and Research Infrastructures for the Development of Networks and Communities, 2006. Tridentcom, 2006, p. 6, http://dx.doi.org/10.1109/TRIDNT.2006.1649137, 134.

[113] J. Armstrong, B.J.C. Schmidt, D. Kalra, H.A. Suraweera, A.J. Lowery, SPC07-4: performance of asymmetrically clipped optical OFDM in AWGN for an intensity modulated direct detection system, in: IEEE Globecom 2006, 2006, pp. 1–5, http://dx.doi.org/10.1109/GLOCOM.2006.571.

[114] R. Mesleh, H. Elgala, H. Haas, Led nonlinearity mitigation techniques in optical wireless ofdm communication systems, IEEE/OSA J. Opt. Commun. Netw. 4 (11) (2012) 865–875, http://dx.doi.org/10.1364/JOCN.4.000865.

[115] H. Elgala, R. Mesleh, H. Haas, Non-linearity effects and predistortion in optical OFDM wireless transmission using LEDs, Inderscience Int. J. Ultra Wideband Commun. Syst. 1 (2) (2009) 143–150.

[116] Z. Ghassemlooy, W. Popoola, S. Rajbhandari, Optical Wireless Communications: System and Channel Modelling with MATLAB®, Taylor & Francis, 2012.

[117] D. Tsonev, S. Sinanovic, H. Haas, Complete modeling of nonlinear distortion in OFDM-based optical wireless communication, J. Lightw. Technol. 31 (18) (2013) 3064–3076, http://dx.doi.org/10.1109/JLT.2013.2278675.

[118] A. Gomez, H. Chun, S. Rajbhandari, G. Faulkner, D. O'Brien, K. Cameron, A.V.N. Jalalakumari, R.K. Henderson, 100 Mb/s wavelength division multiplexing visible light communications link using a triple-junction photo-diode, IEEE Photonics Soc. Summer Top. Meet. Ser. (SUM) (2016) 29–30, http://dx.doi.org/10.1109/PHOSST.2016.7548715.

[119] R.J. Drost, B.M. Sadler, Constellation design for channel precompensation in multi-wavelength visible light communications, IEEE Trans. Commun. 62 (6) (2014) 1995–2005.

[120] R. Singh, T. O'Farrell, J.P.R. David, Performance Evaluation of Ieee 802.15.7 Csk Physical Layer, 2013, pp. 1064–1069. IEEE Globecom Workshops (GC Workshops).

[121] R.Y. Mesleh, H. Haas, S. Sinanovic, C.W. Ahn, S. Yun, Spatial modulation, IEEE Trans. Veh. Technol. 57 (4) (2008) 2228–2241, http://dx.doi.org/10.1109/TVT.2007.912136.

[122] W. Popoola, E. Poves, H. Haas, Generalised space shift keying for visible light communications, In: Proceedings of the 2012 8th International Symposium on Communication Systems, Networks & Digital Signal Processing (CSNDSP).

[123] M. Ijaz, D. Tsonev, J.J.D. McKendry, E. Xie, S. Rajbhandari, H. Chun, G. Faulkner, E. Gu, M.D. Dawson, D. O'Brien, H. Haas, Experimental proof-of-concept of optical spatial modulation ofdm using micro leds, in: IEEE International Conference on Communication Workshop, 2015, pp. 1338–1343.

[124] Z. Chen, N. Serafimovski, H. Haas, Angle diversity for an indoor cellular visible light communication system, in: 2014 IEEE 79th Vehicular Technology Conference (VTC Spring), 2014, pp. 1–5, http://dx.doi.org/10.1109/VTCSpring.2014.7022832.

[125] T.Q. Wang, C. He, J. Armstrong, Angular diversity for indoor mimo optical wireless communications, in: IEEE International Conference on Communications (ICC), 2015, pp. 5066–5071, http://dx.doi.org/10.1109/ICC.2015.7249127.

[126] S. Dimitrov, R. Mesleh, H. Haas, M. Cappitelli, M. Olbert, E. Bassow, On the sir of a cellular infrared optical wireless system for an aircraft, IEEE J. Sel. Areas Commun. 27 (9) (2009) 1623–1638, http://dx.doi.org/10.1109/JSAC.2009.091212.

[127] S. Dimitrov, H. Haas, M. Cappitelli, M. Olbert, On the throughput of an ofdm-based cellular optical wireless system for an aircraft cabin, in: Proceedings of the 5th European Conference on Antennas and Propagation (EUCAP), 2011, pp. 3089–3093.

[128] J. Xu, J. Zhang, J.G. Andrews, On the accuracy of the wyner model in cellular networks, IEEE Trans. Wirel. Commun. 10 (9) (2011) 3098–3109, http://dx.doi.org/10.1109/TWC.2011.062911.100481.

[129] J. Andrews, F. Baccelli, R. Ganti, A tractable approach to coverage and rate in cellular networks, IEEE Trans. Commun. 59 (11) (2011) 3122–3134, http://dx.doi.org/10.1109/TCOMM.2011.100411.100541.

[130] R. Zhang, H. Claussen, H. Haas, L. Hanzo, Energy efficient visible light communications relying on amorphous cells, IEEE J. Sel. Areas Commun. 34 (4) (2016) 894–906, http://dx.doi.org/10.1109/JSAC.2016.2544598.

[131] J.G. Andrews, F. Baccelli, R.K. Ganti, A new tractable model for cellular coverage, in: 48th Annual Allerton Conf. On Commun., Control, and Computing, 2010, pp. 1204–1211, http://dx.doi.org/10.1109/ALLERTON.2010.5707051.

[132] A. Guo, M. Haenggi, Spatial stochastic models and metrics for the structure of base stations in cellular networks, IEEE Trans. Wirel. Commun. 12 (11) (2013) 5800–5812, http://dx.doi.org/10.1109/TWC.2013.100113.130220.

[133] I. Stefan, H. Haas, Analysis of optimal placement of led arrays for visible light communication, in: 2013 IEEE 77th Vehicular Technology Conference (VTC Spring), 2013, pp. 1–5, http://dx.doi.org/10.1109/VTCSpring.2013.6691890.

[134] P. Patel, J. Holtzman, Analysis of a simple successive interference cancellation scheme in a ds/cdma system, IEEE J. Sel. Areas Commun. 12 (5) (1994) 796–807, http://dx.doi.org/10.1109/49.298053.